



NAVAL POSTGRADUATE SCHOOL

MONTEREY, CALIFORNIA

THESIS

**LOCALIZATION OF SURFACE OR NEAR-SURFACE
DRIFTING MINES FOR UNMANNED SYSTEMS IN THE
PERSIAN GULF**

by

Meng Wee Joses Yau

June 2012

Thesis Co-Advisor:

Thesis Co-Advisor:

Second Reader:

Peter C. Chu

Timothy H. Chung

Ronald E. Betsch

Approved for public release; distribution is unlimited

THIS PAGE INTENTIONALLY LEFT BLANK

REPORT DOCUMENTATION PAGE

Form Approved
OMB No. 0704-0188

The public reporting burden for this collection of information is estimated to average 1 hour per response, including the time for reviewing instructions, searching existing data sources, gathering and maintaining the data needed, and completing and reviewing the collection of information. Send comments regarding this burden estimate or any other aspect of this collection of information, including suggestions for reducing this burden to Department of Defense, Washington Headquarters Services, Directorate for Information Operations and Reports (0704-0188), 1215 Jefferson Davis Highway, Suite 1204, Arlington, VA 22202-4302. Respondents should be aware that notwithstanding any other provision of law, no person shall be subject to any penalty for failing to comply with a collection of information if it does not display a currently valid OMB control number. **PLEASE DO NOT RETURN YOUR FORM TO THE ABOVE ADDRESS.**

1. REPORT DATE (DD-MM-YYYY) 8-6-2012			2. REPORT TYPE Master's Thesis		3. DATES COVERED (From — To) 2011-06-01—2012-06-30	
4. TITLE AND SUBTITLE Localization of Surface or Near-surface Drifting Mines for Unmanned Systems in the Persian Gulf					5a. CONTRACT NUMBER	
					5b. GRANT NUMBER N6230611PO00123, N0001412WX20510	
					5c. PROGRAM ELEMENT NUMBER	
6. AUTHOR(S) Meng Wee Joses Yau					5d. PROJECT NUMBER	
					5e. TASK NUMBER	
					5f. WORK UNIT NUMBER	
7. PERFORMING ORGANIZATION NAME(S) AND ADDRESS(ES) Naval Postgraduate School Monterey, CA 93943					8. PERFORMING ORGANIZATION REPORT NUMBER	
9. SPONSORING / MONITORING AGENCY NAME(S) AND ADDRESS(ES) Naval Oceanographic Office Stennis Space Center, MS 39529 - 6000					10. SPONSOR/MONITOR'S ACRONYM(S)	
					11. SPONSOR/MONITOR'S REPORT NUMBER(S)	
12. DISTRIBUTION / AVAILABILITY STATEMENT Approved for public release; distribution is unlimited						
13. SUPPLEMENTARY NOTES The views expressed in this thesis are those of the author and do not reflect the official policy or position of the Department of Defense or the U.S. Government. IRB Protocol Number: N/A						
14. ABSTRACT This thesis investigates the combined use of ocean models, such as idealized surface current flows, and search models, including expanding area and discrete myopic search methods, to improve the probability of detecting a near-surface, drifting object over time. Enhanced search effectiveness is facilitated by the use of robotic search agents, such as a tactical unmanned underwater vehicle (UUV) or unmanned aerial vehicle (UAV), leveraging simulation methods to inform the search process. The presented work investigates the impact of using naive versus optimized search patterns on localizing a drifting object, including a surrogate ocean model using idealized flow as well as historical data sets with Weibull-distributed perturbations. Numerical studies and extensive analysis using different permutations of model parameters (including the relative speed of the drifting object, time late in the searcher's arrival to the search area, sensor sweep width, and duration of the search mission) identify the significant factors affecting the overall probability of detection. Such insights enable further explorations using empirical datasets for specific oceanographic regions of interest.						
15. SUBJECT TERMS Ocean Models, Search Models, Unmanned Systems, Naive Search, Myopic Search, Time Late, Sweep Width						
16. SECURITY CLASSIFICATION OF:			17. LIMITATION OF ABSTRACT	18. NUMBER OF PAGES	19a. NAME OF RESPONSIBLE PERSON	
a. REPORT Unclassified	b. ABSTRACT Unclassified	c. THIS PAGE Unclassified			19b. TELEPHONE NUMBER (include area code)	

THIS PAGE INTENTIONALLY LEFT BLANK

Approved for public release; distribution is unlimited

**LOCALIZATION OF SURFACE OR NEAR-SURFACE DRIFTING MINES FOR
UNMANNED SYSTEMS IN THE PERSIAN GULF**

Meng Wee Joses Yau
Lieutenant Commander, Republic of Singapore Navy
B.Tech., Electronics Engineering, National University of Singapore, 2004

Submitted in partial fulfillment of the
requirements for the degree of

MASTER OF SCIENCE IN PHYSICAL OCEANOGRAPHY

from the

**NAVAL POSTGRADUATE SCHOOL
June 2012**

Author: Meng Wee Joses Yau

Approved by: Peter C. Chu
Thesis Co-Advisor

Timothy H. Chung
Thesis Co-Advisor

Ronald E. Betsch
Second Reader

Jeffrey D. Paduan
Chair, Department of Oceanography

THIS PAGE INTENTIONALLY LEFT BLANK

ABSTRACT

This thesis investigates the combined use of ocean models, such as idealized surface current flows, and search models, including expanding area and discrete myopic search methods, to improve the probability of detecting a near-surface, drifting object over time. Enhanced search effectiveness is facilitated by the use of robotic search agents, such as a tactical unmanned underwater vehicle (UUV) or unmanned aerial vehicle (UAV), leveraging simulation methods to inform the search process. The presented work investigates the impact of using naïve versus optimized search patterns on localizing a drifting object, including a surrogate ocean model using idealized flow as well as historical data sets with Weibull-distributed perturbations. Numerical studies and extensive analysis using different permutations of model parameters (including the relative speed of the drifting object, time late in the searcher’s arrival to the search area, sensor sweep width, and duration of the search mission) identify the significant factors affecting the overall probability of detection. Such insights enable further explorations using empirical datasets for specific oceanographic regions of interest.

THIS PAGE INTENTIONALLY LEFT BLANK

Table of Contents

List of Acronyms and Abbreviations	xvii
1 Introduction	1
1.1 Motivation	1
1.2 Economic Significance of Persian Gulf.	2
1.3 Contributions	3
1.4 Thesis Organization	3
2 Illustrating the Dynamics	5
2.1 Brief History of Mine Warfare	6
2.2 What are Drifting Mines?	7
2.3 Offensive Mine Warfare	8
2.4 Geographic Features of Persian Gulf.	9
2.5 Environmental Factors From Previous Studies	9
3 Model Development	15
3.1 Search Models for Drifting Objects	15
3.2 Ocean Surface Current Models	17
3.3 Integrated Search and Ocean Modeling.	20
4 Analysis of Model Output	25
4.1 Search Analysis Using Potential Flow Model	25
4.2 Statistical Analysis on Potential Flow Model	29
4.3 Search Analysis Using Historical Data Set	31
4.4 Effects of Weibull Probability Distribution Function	48
4.5 Effects of High/Low and High/High Wind/Current Events	50

4.6 Statistical Analysis on Historical Data Set 52

5 Conclusions and Future Work 55

5.1 Simulation Model 55

5.2 Findings 56

5.3 Areas of Future Research 56

Initial Distribution List 63

List of Figures

Figure 2.1	Topographic Map of the Middle Eastern countries centering on the Persian Gulf.	10
Figure 2.2	Sketch of surface currents and circulation processes in the Persian Gulf and western Gulf of Oman (From Reynolds, 1993). The dashed lines in the central part of the gulf indicate the approximate seasonal location of the salinity front between the inflowing fresh water and the more saline waters of the gulf.	11
Figure 2.3	Plot of Wind Amplitudes from Feb to Jul 2006 (From Williams, 2007)	13
Figure 2.4	Illustration of the mean wind vectors for the months of Apr and Jul 2006 as obtained from FNMOC. The northwesterly winds predominantly flow along the major axis while the onset of the southwest monsoon causes a convergence near the SOH (From Williams, 2007)	13
Figure 2.5	Physical characteristics of Persian Gulf. (National Geophysical Data Centre, 2010)	14
Figure 3.1	Five-day mean of the global ocean surface currents measured in meters per second. The plot is produced by OSCAR and the data is centered on December 26, 2011. The plot covers the world oceans from 60°S to 60°N with a resolution of 1°.	18
Figure 3.2	Illustration of simulated uniform potential flow at 1.0 m/s with a generalized source-sink pair, which acts as a bluff body in the flow. An object is dropped at (x,y) coordinate (0.2,1.0) and will follow the $u - v$ velocities (i.e., in flow relative coordinates) created by the composite flow, shown by the magenta line over an evolution of five minutes.	19
Figure 3.3	Weibull(2-Parameter) Plots for different scale factor λ and shape parameter γ (or referred to as k in the plots) parameters (a) Probability Distribution Function and (b) Cumulative Distribution Function (Wikipedia, 2012)	20

Figure 3.4	Illustration of the simulated dispersion of particles in the presence of two-dimensional perturbations over time. These noises are drawn according to a Weibull distribution, which has been shown to model surface current randomness. Depending on the distribution parameters, one can construct (a) a balanced, nearly isotropic dispersion pattern, or (b) a biased dispersion along a preferred dimension, to best model the ocean environment in the region of interest.	21
Figure 3.5	Simulation of a particle cloud is used to define a time-varying search area (i.e., the convex hull enclosing the particle cloud) as it evolves in time. The blue dots represent the locations of the 500 particles at a time late of 36 hours, and the red dotted outline shows the growing search area over each time interval. This area of uncertainty is then decomposed into four partitions, for each of which a prior probability of object presence is computed using the percentage of the total particles contained within.	22
Figure 4.1	Probability of detections from simulation studies comparing linear search (red squares) and myopic search (blue diamonds). The search and ocean parameters are $\tau = 24$ hrs, $W = 500$ m, and object speed ratio is set to (a) $U = 2\%$, which sees linear search improving with increased search times, and (b) $U = 1\%$, where either search method yields nearly perfect detections due to the short time late and large sensor sweep width. . .	27
Figure 4.2	Search mission results for $\tau = 24$ hours, $W = 100$ m, and for (a) $U = 2\%$, and (b) $U = 0.2\%$. For shorter sensing distances and slower surface currents as in (b), the myopic search approach appears to vastly outperform the naïve linear search.	27
Figure 4.3	Search mission results for $\tau = 36$ hours, $W = 500$ m, and for (a) $U = 2\%$, and (b) $U = 1\%$. For faster surface speeds, the myopic search approach suffers initially by too narrowly focusing its search effort, although for both speed ratios, it appears to close the gap in search performance for missions extending past the initial first hour.	28
Figure 4.4	Search mission results for $\tau = 36$ hours, $W = 100$ m, and for (a) $U = 2\%$, and (b) $U = 0.2\%$. Linear search appears to perform better than myopic search no matter the search mission duration when the drifting objects move relatively faster. For slow-moving objects, only after four hours does myopic search begin to perform marginally better.	29

Figure 4.5	An example instance of an alternate initial location of the drifting object, such as below the source-sink pair. The functional dependencies of the probability of detection on the factors presented in this paper appear to hold for arbitrary initial locations.	30
Figure 4.6	Comparison of the mean probability of detection between myopic search and linear search for W of 1000 m, 500 m and 100 m	31
Figure 4.7	Drifter starting locations in north Persian Gulf. Location 1 is situated at 29°N , 49.2°E while location 2 is at 29.5°N , 48.5°E	32
Figure 4.8	Drifter plots, without noise, for $\tau = 24$ hours, on 15 April for (a) location 1, and (b) location 2, as well as on 15 July for (c) location 1 and (d) location 2. The magenta line represents the drifter movement and the * symbol is used to denote the final position of the drifter at the end of 24 hrs.	33
Figure 4.9	Surface current flow on 15 April, for (a) $\tau = 4$ hrs, (b) $\tau = 6$ hrs, (c) $\tau = 8$ hrs, (d) $\tau = 10$ hrs, (e) $\tau = 11$ hrs and (f) $\tau = 12$ hrs. Surface currents tend to flow towards the northwest at semidiurnal periods	34
Figure 4.10	Surface current flowing northwest on 15 April, for (a) $\tau = 24$ hrs and (b) $\tau = 36$ hrs	35
Figure 4.11	Illustration of the difference between using the mean speed (0.53% or 0.265 m/s) and direction (035°) to plot the drifter position in time as compared to using the interpolated speed and direction of the surface currents calculated at five-minute intervals.	35
Figure 4.12	Search results for particle run number 1 starting at location 1 on 15 April for $\tau = 24$ hrs with a variation of W ((a)1000 m, (b)500 m, (c)200 m and (d)100 m) being evaluated. As W reduces, the “greedy” algorithm recommends an alternative search plan that maximizes the detection probability while minimizing the search cost (i.e., time)	37
Figure 4.13	Probability of detections from simulation studies comparing linear search (red squares) and myopic search (blue diamonds). The search and ocean parameters are $\tau = 24$ hours, $W=500$ m, and mean surface current speed or object speed ratio at location 1 (a) $U=0.265\text{m/s}$ (0.53% of V) and at location 2, (b) $U=0.425\text{m/s}$ (0.85% of V). For both cases, there is a crossover point at $T = 2\text{hrs}$ where myopic search performs slightly better than linear search	39

Figure 4.14	Search mission results for $\tau = 24$ hours, $W = 100$ m, and for mean surface current speed or object speed ratio at location 1 (a) $U=0.265\text{m/s}$ (0.53% of V) and at location 2, (b) $U=0.425\text{m/s}$ (0.85% of V). For shorter sensing distances and slower surface currents as in (a), the myopic search approach appears to only outperform the naïve linear search at $T = 4$ hours	39
Figure 4.15	Search mission results for $\tau = 36$ hours, $W = 500$ m, and for mean surface current speed at location 1 (a) $U=0.2725\text{m/s}$ (0.545% of V) and at location 2, (b) $U=0.4315\text{m/s}$ (0.863% of V). For larger search area, myopic suffered more initially but managed to regain its performance past the initial hour. The 58% difference in U had minimal impact on search performance	40
Figure 4.16	Search mission results for $\tau = 36$ hours, $W = 500$ m, and for mean surface current speed at location 1 (a) $U=0.2725\text{m/s}$ (0.545% of V) and at location 2, (b) $U=0.4315\text{m/s}$ (0.863% of V). Linear search outperformed myopic search regardless of the search mission duration and mean U speed	41
Figure 4.17	Probability of detections from simulation studies carried on two locations on 15 July. The search and ocean parameters were $\tau = 24$ hours, $W=500$ m, and mean surface current speed or object speed ratio at location 1 (a) $U=0.265\text{m/s}$ (0.53% of V) and at location 2, (b) $U=0.463\text{m/s}$ (0.926% of V). For both cases, there was a crossover point at $T = 2\text{hrs}$ where myopic search performed slightly better than linear search	42
Figure 4.18	Search mission results for $\tau = 24$ hours, $W = 100$ m, and for mean surface current speed or object speed ratio at location 1 (a) $U=0.265\text{m/s}$ (0.53% of V) and at location 2, (b) $U=0.463\text{m/s}$ (0.926% of V). Myopic search approach appeared to only outperform the naïve linear search at $T = 3$ hours	43
Figure 4.19	Search mission results for $\tau = 36$ hours, $W = 500$ m, and for mean surface current speed at location 1 (a) $U=0.255\text{m/s}$ (0.51% of V) and at location 2, (b) $U=0.443\text{m/s}$ (0.885% of V). Myopic suffered more initially but managed to regain its performance past the initial hour. The 74% increase in U had minimal impact on the search performance . . .	44

Figure 4.20	Search mission results for $\tau = 36$ hours, $W = 500$ m, and for mean surface current speed at location 1 (a) $U=0.255\text{m/s}$ (0.51% of V) and at location 2, (b) $U=0.443\text{m/s}$ (0.885% of V). Linear search outperformed myopic search for search mission duration less than or equal to 3 hours. Myopic search only managed to perform slightly better when the search duration was extended to four hours. The 74% increase in U caused a 5% drop in detection probability	45
Figure 4.21	Search mission results at location 1 for $\tau = 24$ hours, W ranging from 100 m to 1,000 m, and for varying search time with (a) $T = 1$ hour, (b) $T = 2$ hours, (c) $T = 3$ hours and (d) $T = 4$ hours. Linear search outperformed myopic search for all sweep width settings at search mission duration equal to 1 hour with myopic search performing better at $W \geq 400$ m for extended durations. The crossover point where linear search performed better was observed to progressively shift towards W of 300 m when T increased	46
Figure 4.22	Search mission results at location 1 for $\tau = 36$ hours, W ranging from 100 m to 1,000 m, and for varying search time with (a) $T = 1$ hour, (b) $T = 2$ hours, (c) $T = 3$ hours and (d) $T = 4$ hours. Myopic search performed considerably worse than linear search at $T = 1$ hour but started to resemble linear search performance as T was increased to 4 hours	47
Figure 4.23	Search mission results at location 2 for $\tau = 24$ hours, W ranging from 100 m to 1,000 m, and for varying search time with (a) $T = 1$ hour, (b) $T = 2$ hours, (c) $T = 3$ hours and (d) $T = 4$ hours. Linear search performed better at $T = 2$ hours at W of about 500 m. This crossover point shifted down to a W of between 400 and 300 m as T increased to 3 hours	48
Figure 4.24	Search mission results at location 2 for $\tau = 36$ hours, W ranging from 100 m to 1,000 m, and for varying search time with (a) $T = 1$ hour, (b) $T = 2$ hours, (c) $T = 3$ hours and (d) $T = 4$ hours. Linear search continued to dominate at $T = 1$ hour. Same crossover point was observed at W between 400 and 300 m for T greater than 1 hour	49
Figure 4.25	Comparison of detection probability between the original myopic data at location 1 with $\tau = 24$ hours and when the scale factor of the Weibull PDF was increased by 10%	50
Figure 4.26	Comparison of increasing the scale factor of the Weibull PDF at location 1 by 10% for (a) $T = 1$ hour and (b) $T = 4$ hours. Blue diamonds denote the original myopic search results with $\lambda = 1.0$ while red squares denote the myopic search results with $\lambda = 1.1$	51

Figure 4.27	Total mean probability of detection between myopic search and linear search. The nonlinearity drop in detection probability for both search strategies was observed to start from a W of about 400 m to 300 m . . .	53
Figure 4.28	Comparison of the total mean probability of detection with error bars for myopic search and linear search. The error bars overlap at $W \geq 400$ m. Even with a higher standard error for $W \leq 300$ m, there are no overlaps between the two search strategies	54

List of Tables

Table 3.1	List of five factors used in the simulation runs to investigate their impact on search effectiveness	22
Table 4.1	List of values used in the simulation runs to investigate their impact on search effectiveness in the potential flow model for both myopic and linear search strategies	26
Table 4.2	List of factor values that are used in the simulation runs with drifter speed, U , being extracted from the historical data set provided by SWAFS. . .	36
Table 4.3	List of 12 cases and their associated parameters used in the simulation runs based on the historical data set.	38
Table 4.4	Calculated p -value result for the 10 different sweep widths used in the simulation runs. For each sweep width, there are 32 pairs of mean detection probability comparing between myopic search and linear search. Each mean detection probability result was obtained by performing 500 simulation runs. Blank entries denote p -values of < 0.00001 , denoting statistically statistical difference between myopic and linear search methods.	52

THIS PAGE INTENTIONALLY LEFT BLANK

List of Acronyms and Abbreviations

MCM Mine Countermeasure
PDF Probability Distribution Function
SOH Strait of Hormuz
SWAFS Shallow Water Assimilation Forecast System
UAE United Arab Emirates
UAV Unmanned Aerial Vehicle
UUV Unmanned Underwater Vehicle

THIS PAGE INTENTIONALLY LEFT BLANK

Acknowledgements

I am grateful to the Naval Oceanographic Office for funding this thesis research. The research process has indeed been extremely time consuming and at times, exasperating when the Matlab code did not function the way it should. This thesis was completed with the expertise, knowledge, and professionalism of the following people:

Thanks to Mr. Ronald E. Betsch for assuming the role of the Second Reader for my thesis. I would also like to thank Mr. Chenwu Fan for his assistance in computational modeling. To Dr. Timothy H. Chung, I am grateful for his guidance and continued challenges in pushing me to explore new areas that I would never have thought of on my own. I am also grateful to Dr. Peter C. Chu, for your guidance and reassuring manner that gave me the confidence and freedom to work on my research knowing that I am on the right track.

My children, Jamie and James, with their unlimited energy, have constantly reminded me to play more. Finally, the most important person that I would like to thank is my wife, Michelle Lee. Without her enduring support, I would not have been able to complete this journey. I am indeed blessed to have her as my partner for life.

THIS PAGE INTENTIONALLY LEFT BLANK

CHAPTER 1:

Introduction

The prevalence of unmanned systems in their diverse application areas is generating not only new technologies and capabilities, but is also facilitating new application domains that lie at the interface of previously disparate communities. One such interdisciplinary arena is between ocean sciences, search missions modeling, and effective employment of autonomous search agents such as unmanned underwater vehicles (UUVs) and unmanned aerial vehicles (UAVs).

In this context, the search for drifting objects in the ocean represents an exemplar of a mission where optimal execution of the search effort benefits greatly by incorporating information about the ocean surface current and environment. Though the respective communities have recognized the operational value in this integration, further advances in computation, modeling and simulation, as well as robotic sensors are rapidly facilitating its realization. Drifting objects whose motions are induced by surface currents are relevant to both civilian and defense applications, including search for crashed aircraft wreckage (as in Air France 447 [1]), search and rescue operations for disabled vessels [2], or clearance missions for near-surface mines deployed in commercial waterways [3].

In the challenging case of the mine clearance scenario, even if an initial route has been cleared, there is no guarantee that the cleared path will not be “re-disturbed” again by the ocean currents. In such cases, as well as in search and rescue operations, the time necessary to find one or more surface or near-surface drifting mines is a critical measure of performance of any solution strategy. The advent of unmanned systems has created a whole new spectrum for concepts of operations that allow for more timely deployment of assets and the ability to cover a wide area search at diminished expense (either in manpower, risk, or search effort). Any information—either historical or sampled—regarding the ocean surface current in the area of operations can potentially aid greatly in informing the search process and enabling more efficient use of searchers in terms of minimizing the time to find the mine(s).

1.1 Motivation

The Office of Naval Research (ONR) released a Broad Agency Announcement (BAA) in July 2011 to search for an innovative technology solution leading to wide-area detection, classification, localization and tracking of surface and near-surface drifting/oscillating mines and pre-

diction of mine drift from direct environmental observations and ocean models to support tactical planning (ONRBAA11-024). The envisaged concept of operations, as stated in the BAA, utilizes a Mine Drift Tactical Decision Aid (TDA) to predict drift trajectories using real-time environmental observations from ocean model data and other sources such as in-situ environment information retrieved from unmanned systems. The unmanned systems may be equipped with sensors such as Side-Looking Sonars, Airborne Laser Mine Detection System, Synthetic Aperture Radar, Electro-Optics and so on, to perform wide-area search as well as real-time detection, classification and localization of surface and near-surface drifting or oscillating mines. The TDA will also be used to plan the efficacious deployment of the unmanned systems.

The BAA thus presented an excellent opportunity where my research could complement prior work on this topic and provide some insights on the differences in detection probabilities when either naïve or optimized search pattern is employed in localizing drifting objects in the Persian Gulf. The Persian Gulf region was chosen due to its strategic significance in the global oil trade as well as the availability of past historic ocean current data that are readily accessible to test the hypothesis. In addition, part of the research work has been submitted to the 2012 IEEE/RSJ International Conference on Intelligent Robots and Systems (IROS 2012).

1.2 Economic Significance of Persian Gulf

Given that petroleum and petroleum-related products remain central to the stability and growth of the world economies, the strategic significance of the Persian Gulf cannot be overlooked. Two-thirds of the world's oil reserves and over 40 percent of the natural gas reserves are concentrated in the Persian Gulf, a region that is undergoing profound changes both in rapid economic and infrastructural development as well as social and cultural changes. In 2007, 17 million barrels of oil a day passed through the Strait of Hormuz (SOH), which is the equivalent of about 40 percent of all global oil transportation [4].

The U.S. has a vested interest in the stability of the Persian Gulf region and has continually forward-deployed its Naval forces there for the past thirty years to “provide persistent maritime dominance, power projection and effective crisis response” [5]. However, regional tensions continue to rise, which may lead to the destabilization of the region. The future of Iraq, the Arab-Israeli conflict, asymmetric threats including terrorism, and the role of Iran may once again bring the region into chaos [6].

The events of the last decade have demonstrated that Iran, the preeminent indigenous power

in the Persian Gulf, has become a major and indispensable political player in both Iraq and Afghanistan, where the United States is militarily involved. Because of this, Washington cannot formulate policies to these conflicts without taking into consideration Iranian interest [7]. Notwithstanding, Iran is defiant in its quest for nuclear power and has repeatedly stated that any hostile actions taken by the international community, specifically the U.S. or Israel, may result in the closure of the SOH. Iran's threats to disrupt oil have come from as high up as Supreme Leader Ayatollah Ali Khamenei. If any country attacks Iran, "shipment of energy from this region will be seriously jeopardized," Ayatollah Khamenei said in a June 2006 speech. Given the volatile environment surrounding the Persian Gulf region, the possible closure of SOH due to mines is very real.

1.3 Contributions

The main contributions of this thesis include the modeling and simulation of time-varying search areas that incorporate ocean models, which can be used to inform and improve the search for drifting objects by tactical unmanned systems. The search problem formulation, extensive simulation studies, and subsequent statistical analysis provide insights into how to incorporate real-time and/or historical oceanographic data to maximize the probability of detection.

1.4 Thesis Organization

- Chapter 2 provides a glimpse into the world of mine warfare as well as a brief description on the geographic features and environmental factors that surrounds the Persian Gulf.
- Chapter 3 describes the analytic models and relevant works for both search operations and ocean surface currents.
- Chapter 4 investigates the integration and implementation of the model and discusses the results and statistical insights obtained from this study.
- Chapter 5 discusses the implications of the experimental results as well as recommendations for future avenues of research.

THIS PAGE INTENTIONALLY LEFT BLANK

CHAPTER 2:

Illustrating the Dynamics

Mines are relatively low-cost and highly effective weapons that are used to impose sea control by neutralizing or destroying enemy ships as well as interrupting sea lines of communication by preventing the passage through an area of sea. The U.S. Navy uses three categories to classify mines according to how they are deployed in the water. The categories are bottom, moored and drifting mines. Bottom mines have negative buoyancy, sink to the bottom of the ocean and stay there. Moored mines have their explosive charge and firing mechanism housed in a positively buoyant casing and tethered to an anchor on the sea bottom. The length of cable can be preset to ensure that the mines are deployed at the predetermined depth. Drifting mines are mines that float freely at or near the surface of the water.

Psychologically, just the threat that mines exist in an area can easily deter an enemy from deploying his naval forces unless the area has been swept by mine sweepers and declared safe for transit. Similarly, shipping companies will not want to risk transporting their goods through these dangerous waters, and this may result in delays with the shipping schedules as ships may be required to make a detour via an alternate route or to call at an alternate port to unload their goods. While international law requires nations to declare when an area is mined, the warnings need not have to be specific. For example, during World War II, Britain simply declared that it had mined the English Channel, the North Sea and the French coast in order to deter the German invasion.

If a rogue nation or terrorist group was able to obtain or build a series of contact mines that are currently considered as design relics from World War I and deployed these mines randomly, it would effectively choke an entire body of water as no ships will be able to sail through the mined waters without a Mine Countermeasure (MCM) vessel to lead the way. If these mines were allowed to drift at or near the surface with prevailing currents in the same body of water, then they would present an alarmingly difficult and time consuming problem for MCM search analysts to track down and dispose of each and every mine. Even if an initial route has been cleared, there is no guarantee that the cleared path will not be “mined” again by the natural ocean currents.

2.1 Brief History of Mine Warfare

Mine warfare began in 1776 when David Bushnell invented the “Bushnell’s Keg.” These kegs were placed in the Delaware River so that they would float into British ships downriver. These early mines were called torpedoes. In fact, when Admiral Farragut said “Damn the torpedoes” at the Battle of Mobile Bay, he was actually referring to mines [8].

When the American Civil War broke out in 1861, the Confederate forces did not have a comparable naval force that could match the Union side. Given their limitations in constructing conventional coastal defenses, the Confederates chose defensive mining to defend their ports and coastal cities. At the end of the war, a total of forty-three Union ships were struck by the Confederate mines, twenty-seven of which sank.

During World War I, mines again played an important role in the naval battle. The allied forces sowed a 250-mile wide minefield between Scotland and Norway to stop the German U-boats. This minefield was planted in five months during 1918 by American and British ships and contained over 72,000 mines.

During World War II, influence mines (using a combination of magnetic, pressure and acoustic sensors) were developed by the Germans. The small number of influence mines laid by Germany in 1939 virtually brought the infested ports to a standstill until sweeping techniques could be developed. Mines were used by all sides throughout World War II, and surface ships were fitted with paravanes to fend off contact mines. In Japan, *Operation Starvation* saw U.S. Army B-29 aircraft sowing more than 12,000 mines around Japanese shipping routes and harbor approaches, sinking 650 ships and choking off all maritime shipping [8].

On the other hand, the U.S. minesweepers and minelayers were primarily used for defensive mining operations, protecting friendly harbors from enemy infiltration. Thousands of these mines were laid outside Chesapeake Bay, around Cape Hatteras, and at Key West to protect U.S. shipping against enemy submarines. In addition, large mine fields were laid in the Atlantic, off the coasts of Trinidad and North Africa as well as in the Mediterranean. While there is no record of any enemy ships being sunk or damaged in these mine fields, neither is there any record of any enemy ships passing through these fields.

It was perhaps the knowledge that the mine fields existed in these areas in the first place that deterred the enemy from making any attempts to transit through these areas at all. During the Korean War, American forces were prevented from landing at Wonsan for over a week in

1950 until 3,000 Communist mines could be cleared. Similar tactics were used again during the Vietnam War, when the Vietcong planted numerous mines made from modified bombs in shallow rivers and deltas to disrupt shipping.

Throughout the history of the U.S. Navy, there were more ships damaged or lost to mines than missiles [9]. During the Korean War, mines laid by North Korean forces damaged 11 U.S. naval vessels. During the Iran-Iraq War, an Iranian M-08 mine costing \$1500 was able to put a 25-foot (8 m) hole in the hull of the USS Samuel B. Roberts (FFG-58), forcing the ship to seek temporary repairs in a dry dock in Dubai, UAE and causing a whopping 96 million dollars in damage [10]. During the Persian Gulf War, both surface and air mine countermeasures forces were deployed to find and neutralize primitive Iranian mines. Two U.S. navy vessels (USS Princeton [CG-59] and USS Tripoli [LPH-10]) were severely damaged by Iraqi mines laid in areas previously thought to be safe for transit.

2.2 What are Drifting Mines?

Mines come in two general varieties: contact and influence. For detonation, contact mines require a physical impact between the target and the mine itself, and are either moored in the mid-water region to an anchor on the bottom, or simply set adrift until they encounter a target. A drifting mine is simply a floating mine without any mooring. These mines usually weigh about 120 kg, including 80 kg of explosives (TNT).

Drifting mines were occasionally used during World War I and World War II. However, they were more feared than effective. After World War I, the drifting contact mine was banned, but continued to be used during periods of sea conflict. The drifting mines were much harder to remove after the war and they caused about as much damage to both sides. According to the terms of the Hague Convention, when mines break away from their moorings and become drifting mines, their design should deactivate the arming mechanism and render the mine inert.

However, in practice, one cannot take this for granted as there is possibility that after several years at sea, the deactivation mechanism might no longer function as intended. In such situations, the mines may become active again and pose a danger to merchant shipping as well as civilians when swept ashore. Such danger still persists in present time and the UK Department for Transport issued an updated notice (Marine Guidance Note MGN 323 (M+F), “Explosives Picked Up At Sea”) to all mariners in 2006 on the hazards that these explosives pose.

2.3 Offensive Mine Warfare

Mine warfare can be classified into offensive and defensive mine warfare. Forces that use offensive mine warfare always have the initiative and the upper hand while the mine countermeasures groups are the underdogs who are constantly seen as responding to those initiatives. The following paragraphs will take a look at three types of offensive mine warfare that a rogue nation or terrorist groups may employ against a superior naval force like the U.S.

2.3.1 Interdiction

In mine warfare terms, the use of mines for interdiction involves the obstruction of shipping lanes and transit points with the intention to restrict the ability of hostile forces to mount attacks from the sea or to inhibit the free flow of commerce or supply routes [11]. In many cases of interdiction mining, the minefields are covertly laid off enemy ports or assets. Once such a minefield is discovered, the port in question is sealed off until all the mines have been swept. It is thus a massive effort required of the mine countermeasures vessels to carry out routine surveillance at every port, on all shipping routes, all of the time.

2.3.2 Attrition

Attrition can be defined as the art of mining High Value Units into a selected area or preventing them from getting to sea. Examples of HVUs are an aircraft carrier or a ballistic missile submarine. Usually attrition is achieved by selecting a suitable choke point through which the High Value Units need to pass and then mining it. In the world today, many nations have a submarine force of two to three boats. If these boats are unable to get out of port, then all the investment placed in acquiring, supporting and maintaining that force would have been wasted and that nation's submarine force is effectively nullified by mines.

2.3.3 Terrorism

A minefield sowed by terrorist groups can consist of as little as a single covertly placed mine or random sowing of mines in a trade route. The terrorist's main objective is not the destruction of ships but the economic damage that follows as a result of disruption to trade and the political fallout between the government and its citizens for failing to keep the waters safe. The business community and the general public, suffering from the economic devastation of the trade disruption, may then add pressure on the government to change their laws or policies, which will eventually favor the terrorists.

2.4 Geographic Features of Persian Gulf

The Persian Gulf, also known as the Arabian Gulf, is a shallow, semi-enclosed basin situated in an arid zone where evaporation greatly exceeds precipitation and river runoff. The Persian Gulf is approximately 990 km long, with a minimum width of about 56 km and maximum depth of 100 m near the SOH, a maximum width of about 338km, and a mean depth of about 35m in the middle of the gulf. The inland sea occupies an area of approximately 251,000 km². River inflows are mostly in the northern end of the gulf, primarily on the Iranian side, with the largest being the Shatt-Al-Arab, a river formed by convergence of the Tigris, Euphrates, and Karun rivers.

The gulf is surrounded by the deserts of the Arabian Peninsula to the west and the Zagros Mountains of Iran to the east (shown in Fig. 2.1). Iran's Zagros Mountains begin in northwestern Iran and end in the southern province of Hormozgan, north of SOH. These mountains act to channel the winds to the southeast. Thus, the Persian Gulf is characterized by northwesterly or westerly winds throughout the year with mild and continuous summer winds as well as sudden and violent winds in the winter that are associated with synoptic weather systems [12]. Furthermore, the shallow water in the Persian Gulf means that the difference between the wind-driven current at the surface and sea bottom is minimal and the current flow can be approximated by two-dimensional flow plots [13]. This thesis will focus on the northern Persian Gulf region that is separated from the southern region by a front off Qatar.

2.5 Environmental Factors From Previous Studies

There are three primary contributors to mixing in the water column: (1) tides, (2) winds and waves, and (3) evaporation. Internal waves at density interfaces, and topographic features such as islands, also contribute to mixing, but their contribution is unknown and probably small [12]. The kinetic energy of the water velocity as a result of these factors can be partitioned among the three primary contributors in the approximate ratio of 100, 10 and 1, respectively [12]. However, each factor has a different scaling time: tides vary every few hours at diurnal periods, wind-driven currents vary over a few days, and density-driven currents or thermohaline circulation varies over a period of weeks.

The strong tidal currents create a bottom, mechanical, turbulent friction layer. The enhanced turbulent mixing homogenizes the water column from the bottom up, and a bottom mixed layer is evident in all hydrographic sections. The other two mechanical mixing processes are strongest



Figure 2.1: Topographic Map of the Middle Eastern countries centering on the Persian Gulf.

at the surface. Wind friction creates a surface shear layer and also creates surface wave fields, both of which form a surface mixed layer.

The currents in the northern portion of the Persian Gulf are dominated by northwesterly winds that vary in speed from 10 to 15 knots. Together with freshwater discharge from the Shatt-al-Arab, this creates a southeastward-flowing coastal current along the Arabian and Iranian coasts as shown in Fig. 2.2. Residual currents indicate a surface inflow of the Indian Ocean Surface Water into the Persian Gulf as well as a deep outflow of the Persian Gulf through the SOH.

During winter (January-March), the surface water flowing along the Iranian coast seems to form an anticlockwise gyre or basin-wide cyclonic circulation in the southern half of the Gulf. With the onset of the southwest monsoon in summer (July-September), the current becomes progressively stronger and penetrates far into the northern gulf because of the strengthening stratification, increasing inflow and weakening winds. The evaporation of fresh water enhances mixing by increasing the salinity and density of the surface water, thus reducing surface stability. The combined cooling and evaporation increases the density sufficiently to overturn the water column and creates a well-mixed water column north of Qatar. The circulation in the Persian Gulf is therefore highly dependent on the reversal of the monsoon [14].

Other factors that may affect water circulation in the Persian Gulf are the Coriolis force, river

runoff, bottom topography and coastline boundaries. The effect of the Coriolis force is to deflect the surface inflow towards the Iranian coast and the subsurface outflow towards the Arabian coast. The influx of fresh water is seasonal and localized close to the water sources at the northwest region as well as along the Iranian coast [15].

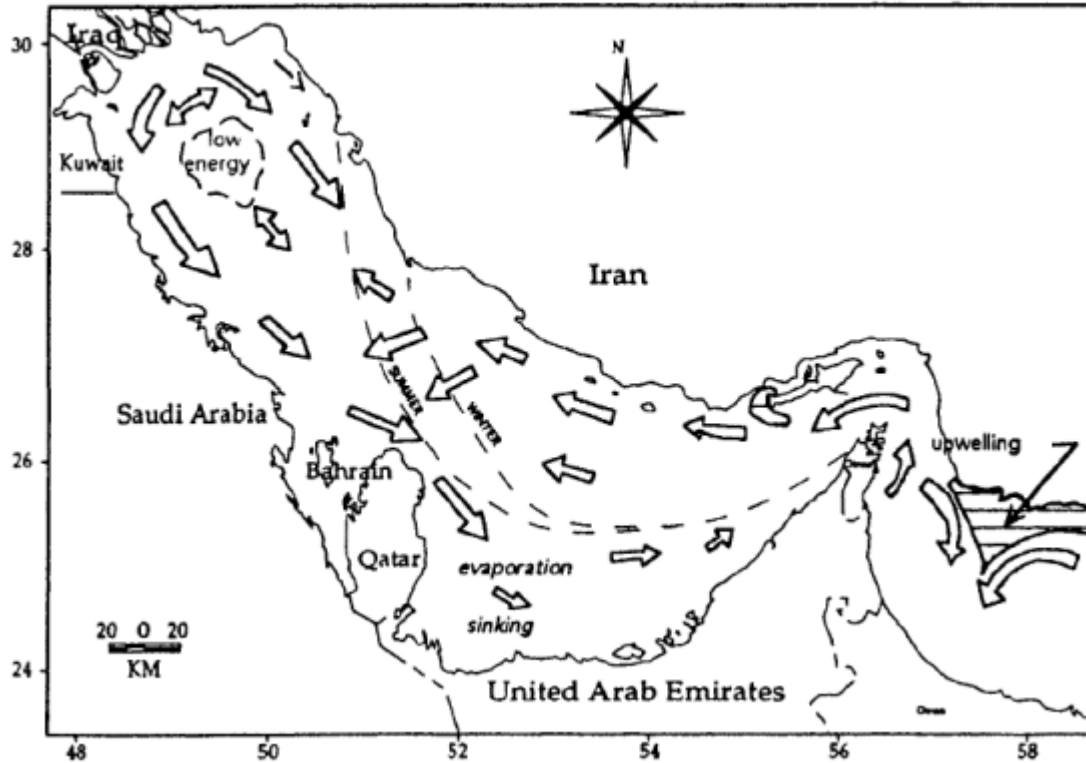


Figure 2.2: Sketch of surface currents and circulation processes in the Persian Gulf and western Gulf of Oman (From Reynolds, 1993). The dashed lines in the central part of the gulf indicate the approximate seasonal location of the salinity front between the inflowing fresh water and the more saline waters of the gulf.

2.5.1 Tides

The tides in the Gulf are complex standing waves and the dominant pattern varies from being primarily semi-diurnal to diurnal. The tidal range is large, with values greater than 1.0 m everywhere [12]. Tides are important for stirring and mixing waters vertically and on a horizontal scale of 10 km, but tides are not an important contribution to the overall circulation in the Persian Gulf. The tidal influence was found to be minimal (less than 2 cm/s), except in a few localized areas (e.g., the Iranian coast and the SOH) where the tidal residuals are large enough to enhance the dominant density-driven flow [16]. Tidal current (averaging longer than a day) has negligible residual energy, and as a result, basin-scale advection from tides is not consid-

ered by most circulation models. Tides are, however, important on smaller scales of horizontal length (< 10 km) and time (< 24 hrs).

2.5.2 Winds

Low-level winds in the Persian Gulf are dominated by land–sea breeze circulation that varies seasonally and diurnally. In summer, the sea breeze is deeper and wider than in winter while on a diurnal scale the intense temperature difference between the land and water surfaces during the daytime and night causes the land–sea breeze circulation to add a landward component to all winds. Over the north coast, the opposing ambient wind creates a sea breeze front that has very limited landward penetration. At the south coast, the penetration is over 250 km [17].

A study by Zhu and Atkinson showed that in January, wind direction at Kuwait International Airport (KWI) was predominantly northwesterly. In January, the direction of the mean wind was clearly from the northwest, but on some occasions the wind blew from the east. In April, the direction of the daytime mean wind was from the east and southeast, i.e., from the sea. In July, the mean direction was again from the northwest throughout the day. The October pattern was rather similar to that in April.

An analysis of each month's characteristics was carried out by Williams using the wind dataset obtained from Fleet Numerical Meteorology and Oceanography Center (FNMOC) and the mean wind speed of about 5 m/s as shown in Fig. 2.3 was shown to flow along the major axis [18]. As the winds progress down the major axis of the Persian Gulf, their magnitudes tend to increase due to the decreased friction from the land–sea breeze circulation winds and the downslope wind flow off the Zagros Mountains to the east.

April's mean wind currents shows the winds flowing predominantly along the major axis with the winds traveling along the Zagros Mountains converging and enhancing the flow in the Persian Gulf as shown in Fig. 2.4(a). With the onset of the southwest monsoon, there is a strong area of convergence near the SOH with the majority of the flow moving towards the Arabian Peninsula. In the northern Persian Gulf, the areas of weak winds also increase to moderate flow as illustrated in Fig. 2.4(b). One thing to note is that both figures indicate the presence of strong offshore winds.

2.5.3 Density

The Persian Gulf Water is one of the most saline water masses in the world. It is formed due to excessive net fresh water loss to the atmosphere through evaporation and constricted

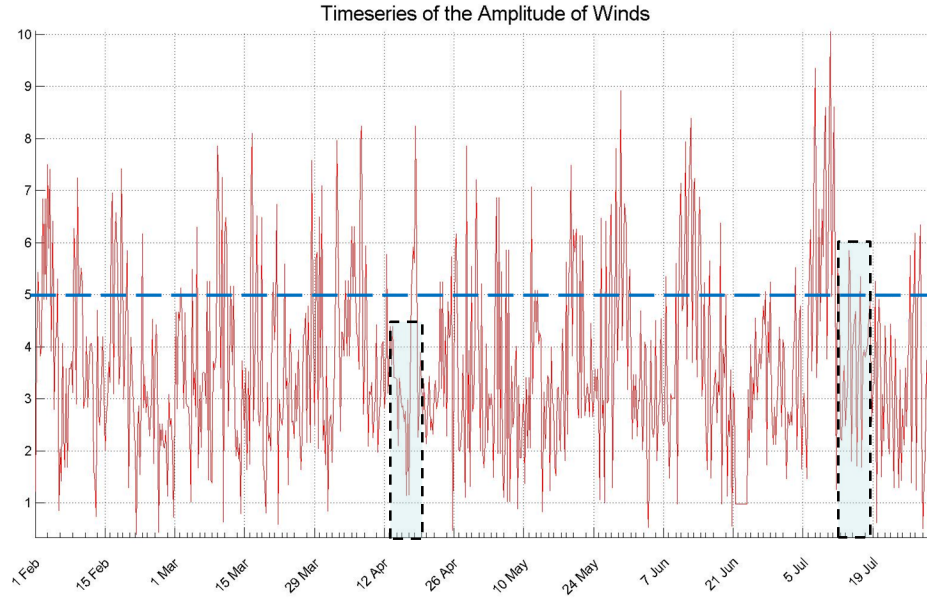


Figure 2.3: Plot of Wind Amplitudes from Feb to Jul 2006 (From Williams, 2007)

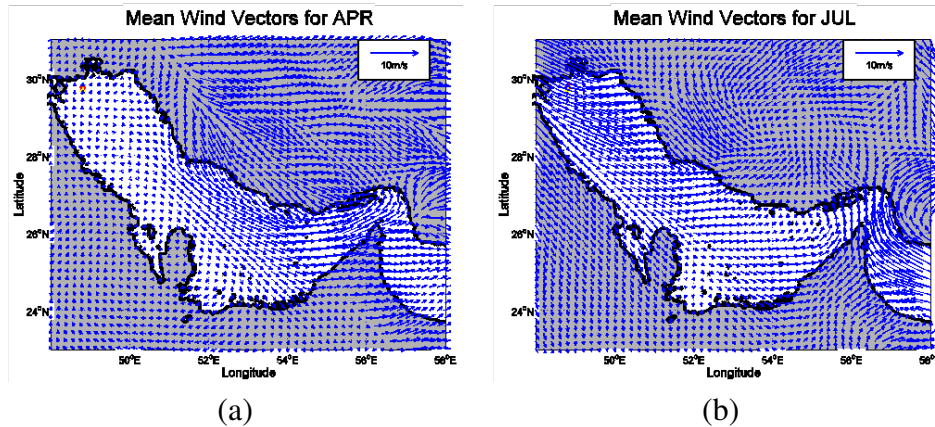


Figure 2.4: Illustration of the mean wind vectors for the months of Apr and Jul 2006 as obtained from FNMOC. The northwesterly winds predominantly flow along the major axis while the onset of the southwest monsoon causes a convergence near the SOH (From Williams, 2007)

water exchange with the open ocean through the SOH due to the much shallower depths of the basin, wider strait to the open ocean and lack of a distinct sill as shown in Fig. 2.5. The rate of vertical mixing is highest in the SOH where numerous topographic features constrict the channel, accelerating tidal flows and generating large eddies capable of scouring the seafloor.

The dense Persian Gulf Water exits the gulf as a deep outflow and induces an inverse estuarine-type water exchange through the SOH. The low salinity Indian Ocean Surface Water spreads

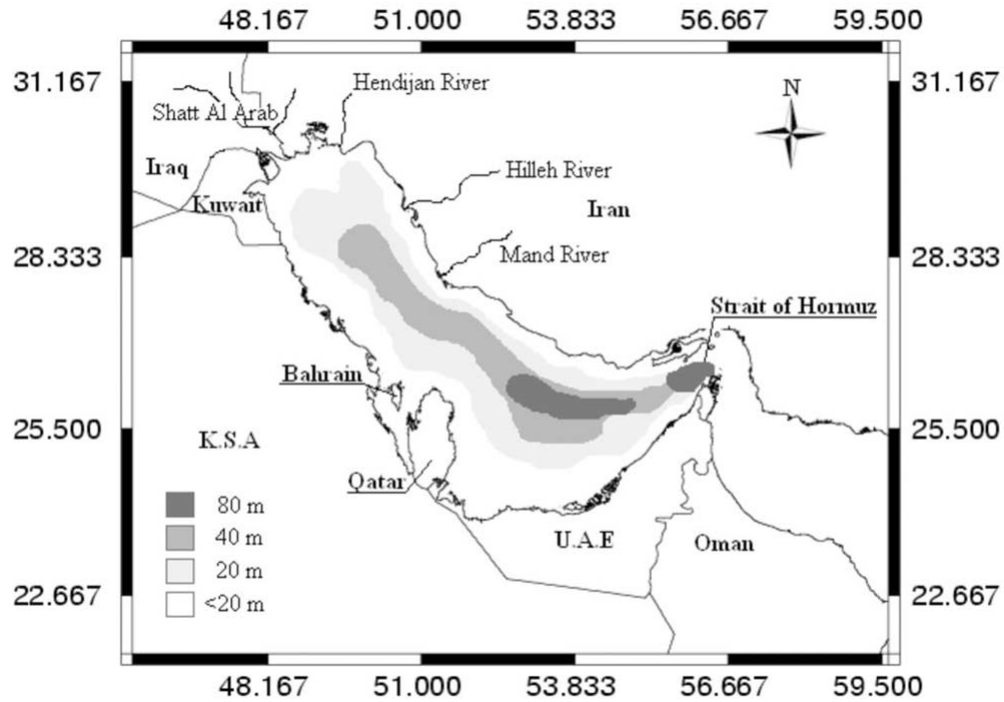


Figure 2.5: Physical characteristics of Persian Gulf. (National Geophysical Data Centre, 2010)

into the interior of the basin generally in two pathways: one branch (northern branch) propagates along the Iranian coast and in summer can reach the basin west of Qatar to form a cyclonic circulation there. It drives a returning coastal current along the Arabian coast north of Qatar. The other branch (southern branch) veers southward to cross the basin to reach the southern UAE coast and also forms an overall cyclonic circulation in the southern gulf [19].

In summer, the vertical mixing is suppressed by the stable thermocline and penetrates to a depth of about 30 m, allowing the Indian Ocean Surface Water to extend farther into the gulf without being greatly modified. In winter, the strong vertical mixing induced by the heat loss leads to an upward salt flux that causes the water column to be well mixed vertically to a depth of about 70 m [20]. The densest water forms during winter in shallow water at the northern end of the gulf. High salinity water forms along the western and southern Arabian coastlines, but the highest densities are not observed there because winter temperatures are milder than those in the north and considerable dilution occurs before high salinity water formed in shallow bays reaches the main gulf basin [21].

CHAPTER 3:

Model Development

3.1 Search Models for Drifting Objects

The mathematics of searching for objects in motion has an extensive theoretical heritage in the operations research community [22], and models for addressing expanding search areas as a result of moving objects (such as a fleeing submarine) have been well-studied in contexts called the “flaming datum search” problem [23]. Additionally, numerous efforts have recently examined the employment of robotic search agents, such as unmanned aerial vehicles equipped with sensors, including works by [24] and [25]. Among others, these works highlight the advantage that even a myopic search strategy of greedily maximizing the detection probability can provide in improving the time efficiency of the search. This section briefly describes these two search methodologies that are relevant to the desired search for drifting objects.

3.1.1 Expanding Area Search

In search problems where the search area grows with time, the challenge of conducting a search in this expanding area becomes evident as the searcher often cannot “keep up” with the rate of area expansion. An example of this is an instance of the flaming datum search problem, where an otherwise concealed submarine makes its location known (e.g., by shooting a missile) at an instant in time before submerging and fleeing from that location. Given the uncertainty in the submarine’s heading in the 2D plane, coupled with the time necessary to get a search asset on station (known as the *time late* and denoted τ), the area where the submarine could possibly be is encapsulated by a *farthest-on circle*. This area grows (assuming constant maximum speed, U , of the target) quadratically in time, whereas the searcher’s ability to sweep this area is only linear. As such, the probability of detection, P_D , of finding the target as a function of time can be approximately bounded between $P_D^{\text{random}} \leq P_D(t) \leq P_D^{\text{ideal}}$, where P_D^{random} and P_D^{ideal} are the cumulative detection probabilities when using a random and ideal coverage strategy, respectively [26]:

$$P_D^{\text{ideal}}(t) = \frac{VW}{\pi U^2} \left(\frac{1}{\tau} - \frac{1}{\tau + t} \right), \quad (3.1)$$

$$P_D^{\text{random}}(t) = 1 - \exp \left(-\frac{VW}{\pi U^2} \left(\frac{1}{\tau} - \frac{1}{\tau + t} \right) \right), \quad (3.2)$$

where V is the searcher speed and W is the sensor sweep width.

Examples of ideal search patterns are lawnmower or spiral patterns that methodically cover the search area. Although these analytic models are useful for gaining an intuition of the relevant search parameters, in realistic conditions where the expanding area is not a symmetric shape, e.g., due to ocean currents and eddies, other approaches must be utilized to compute the time-varying area expansion.

3.1.2 Discrete Myopic Search

The aforementioned random and ideal search strategies do not use prior information about the spatial likelihood of target presence to inform the search path. In contrast, methods such as the discrete myopic search approach [26] leverage such information to good advantage. Discrete myopic search is used to allocate opportunities to conduct a “unit of search” or a *look*. The associated algorithm maximizes the probability of detecting a target by always looking in the region that yields the highest increment in probability of detection. For discrete looks, a locally optimal plan that maximizes the probability of detecting the target can be shown to result in a locally optimal plan that minimizes the mean cost (e.g., time) to find the target [27], which makes it a viable approach in the search for time-sensitive objects.

A given search area (though possibly expanding) is first discretized into n cells in which a probability that a target is within the i^{th} cell, denoted p_i , is assigned. A budget of K looks is available for allocation among these cells. Each successive look in cell i has a probability β_i of not detecting the target, with each look assumed independent of all other looks. Given k_i looks, for $k_i \in \{0, 1, \dots, K\}$, in the i^{th} cell, the objective is to maximize the probability of detection as defined by:

$$P_D = \sum_{i=1}^n p_i (1 - \beta_i^{k_i}), \quad (3.3)$$

subject to nonnegative integer decision variables, k_i , and a constraint on the total number of looks, i.e., $\sum_{i=1}^n k_i \leq K$ and $\sum_{i=1}^n p_i = 1$ [26].

The myopic search algorithm outlines a procedure for allocating each look, for which the $k+1^{\text{st}}$ look, is assigned to the cell with the highest increase in the overall probability of detection, and as such, is a “greedy” algorithm (i.e., steepest gradient ascent). Global optimality is ensured, in the absence of false positive detections, due to the concavity of the objective function in k_i [26]. We leave for future study the impact of false alarms on the searcher’s effectiveness [28] (e.g., if the searcher is penalized for not classifying the mine-like object) and the use of more advanced

search strategies that take into consideration the inherent uncertainty in sensor performance (e.g., multiscale adaptive search algorithm for single or multiple searchers [29]).

3.2 Ocean Surface Current Models

3.2.1 Computational Ocean Nowcast/Forecast Models

Current computational ocean models generally use a number of methods (e.g., climatology, satellite imagery, and in-situ measurements using sensor floats and buoys) to improve their accuracy in predicting the ocean environment, including its temperature, salinity, and, important for our study, surface current speeds. For example, combining satellite data assimilation with existing ocean nowcast/forecast systems has shown to provide a better estimate of sound velocity profiles, which depend on the temperature, salinity, and pressure of the water column [30]. The Persian Gulf is the region of interest to both science and military communities and has been heavily studied and modeled [12, 31].

Accessible from the National Oceanic and Atmospheric Administration's (NOAA) website, the Navy Coastal Ocean Model (NCOM) is the Navy's real-time operational global nowcast/forecast system developed by the Naval Research Laboratory that is built on the base of the Princeton Ocean Model (POM) [32]. The NCOM produces forecasts at three-hour intervals out to 72 hours in the future. Atmospheric forcing is provided by the Navy Operational Global Atmospheric Prediction System (NOGAPS) while the Ocean Surface Current Analyses - Real time (OSCAR) model provides near-real-time global ocean surface currents derived from satellite altimeter and scatterometer data. These models provide a data resolution ranging from 1 degree to as high as 1/3 degree increments. An example of a surface current plot generated from OSCAR is shown in Fig. 3.1.

3.2.2 Simplified Ocean Flow Modeling

The extreme complexity of the computational models described above arises from the immense number of state variables and parameters necessary for high-fidelity models. However, the long time necessary to generate surface current predictions using these models limits their value in tactical or short-time horizon scenarios. Specifically, in the context where we seek to minimize the time late to execute the search, time delay for these forecast models may render the search for drifting objects untenable.

Alternatively, we consider the use of analytic models from two-dimensional potential flow analysis (e.g., for incompressible flow in fluid dynamics) that provide closed form expressions for

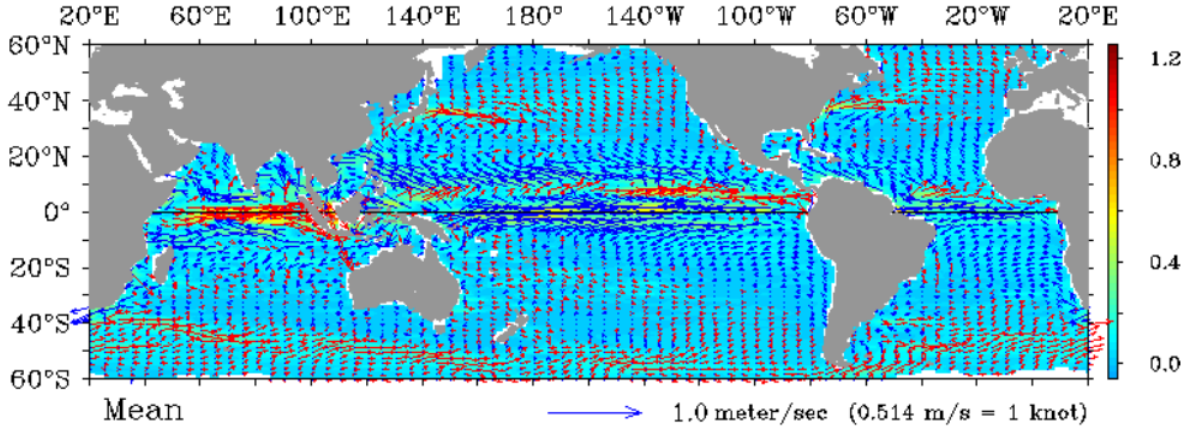


Figure 3.1: Five-day mean of the global ocean surface currents measured in meters per second. The plot is produced by OSCAR and the data is centered on December 26, 2011. The plot covers the world oceans from 60°S to 60°N with a resolution of 1°.

various elementary flow types, such as uniform flow, sources, sinks, vortices, and their various superpositions. These potential flow models can be used and solved in computationally expedient manners (i.e., by solving Laplace’s equation) to provide a surrogate for sophisticated but expensive computational predictions. Additionally, the flexibility of potential functions is such that they can readily be used to construct an approximation to empirical historical data, which can then inform the search process in the methods presented in this thesis.

As an illustrative example, consider a simulated surface current generated by a uniform flow in the presence of a generalized source-sink pair illustrated in Fig. 3.2. The ideal flow field lines identify the paths (assuming no noise) that a drifting particle would take for arbitrary initial conditions. For example, for an object dropped at location marked “1,” its subsequent trajectory will follow the darkened path in time.

3.2.3 Particle-based Expanding Area Simulation

The above potential flow models serve as computationally efficient surrogate surface current models, and can be used to simulate trajectories of a cloud of particles moving in time through the field. However, the idealized flow models do not capture the stochasticity present in real ocean currents. To address this determinism, we can introduce perturbations of the particle paths at each time step, such that the noise causes random dispersions of the particle cloud. In this manner, Monte Carlo simulations using a large number of particles can be used to rapidly approximate the expanding area in which a drifting object could be present, by taking the convex hull of the point cloud as it evolves in time.

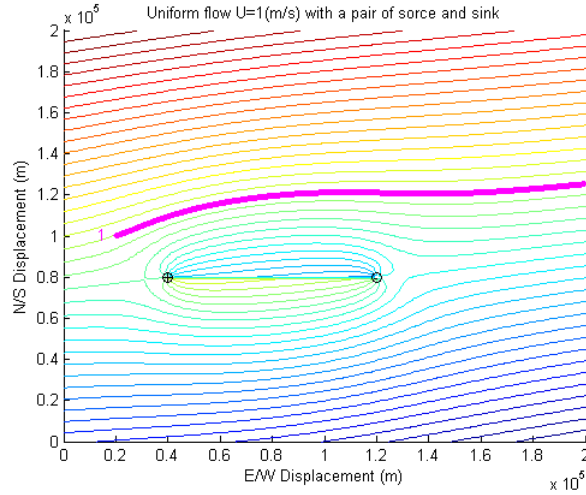


Figure 3.2: Illustration of simulated uniform potential flow at 1.0 m/s with a generalized source-sink pair, which acts as a bluff body in the flow. An object is dropped at (x,y) coordinate $(0.2,1.0)$ and will follow the $u-v$ velocities (i.e., in flow relative coordinates) created by the composite flow, shown by the magenta line over an evolution of five minutes.

In the simulation model presented in this thesis, 500 particles are initialized in the flow field. As time evolves, Weibull-distributed perturbations are added to the particles' positions as their trajectories are simulated using the potential flow velocities. The primary motivation for the use of the Weibull distribution is that it has been shown [33] that the probability distribution function (PDF) of the surface current speeds generally follows a Weibull distribution. Based on the simulated dimensions, the selected Weibull distribution parameters include a scale factor $\lambda = 1.0$ and a shape parameter, $\gamma = 1.5$ for each coordinate (See Fig. 3.3), which appear to produce noise distributions consistent with the previous study.

Fig. 3.4 depicts the resulting particle cloud evolutions in the absence of translational flow for different configurations of the Weibull distribution parameters. These differences cause biases in x and y dimensions, leading to different spatial dispersions. Note that the position of every particle is translated by the centroid coordinates of the point cloud to represent simulated motion in all coordinate (including negative) directions.

The enclosing convex hull is formed by the (red) lines, which corresponds to the expanding area, which can then be used in place of the circular expanding area formulas described in the previous section.

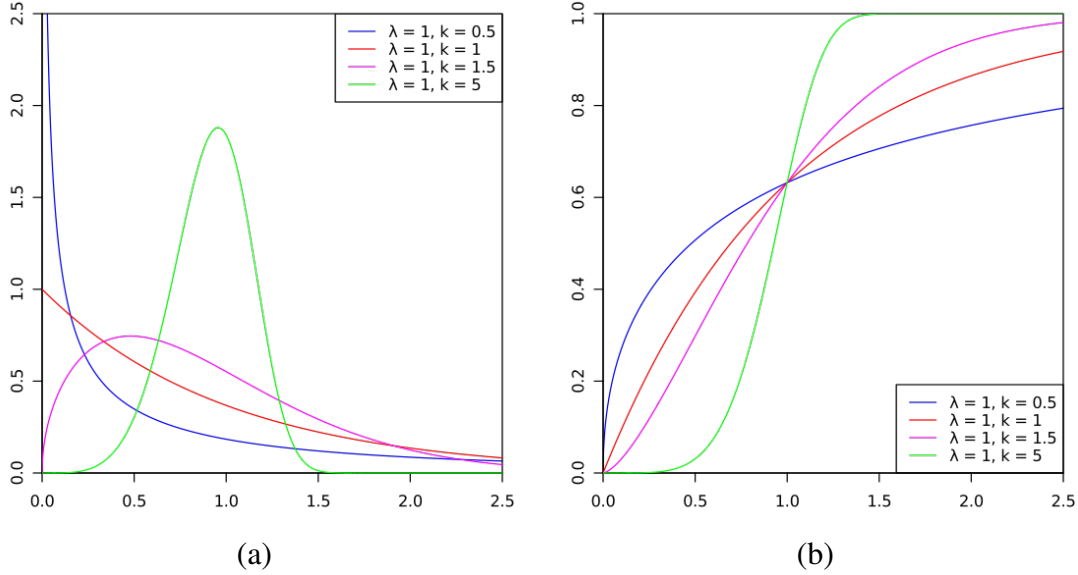


Figure 3.3: Weibull(2-Parameter) Plots for different scale factor λ and shape parameter γ (or referred to as k in the plots) parameters (a) Probability Distribution Function and (b) Cumulative Distribution Function (Wikipedia, 2012)

3.3 Integrated Search and Ocean Modeling

3.3.1 Simulation Scenario Setup

Assume the region of interest where search for drifting objects is in relatively shallow water, such that the (most likely wind-driven) current flow is adequately approximated by 2D flows at the surface. Consider a 200 km by 200 km region of interest where search operations are likely to occur. The scenario commences when a report is received identifying the known time and initial location of a drifting object (e.g., last known position of a downed aircraft, human intelligence of a near-surface mine deployment). At the time of receipt of the report (which may already reflect delayed information), a tactical unmanned aerial sensor platform is deployed to conduct search, but has to contend with additional time late before arriving on station. The searcher will employ its given search strategy, and begin execution of the search upon arrival to its designated start point.

The objective of the investigation presented in this thesis can now be stated as:

Given a (surrogate) surface current flow model and its resulting prediction of the expanded search area for a drifting object with known initial position, how does the choice of search strategy affect the probability of detecting the object?

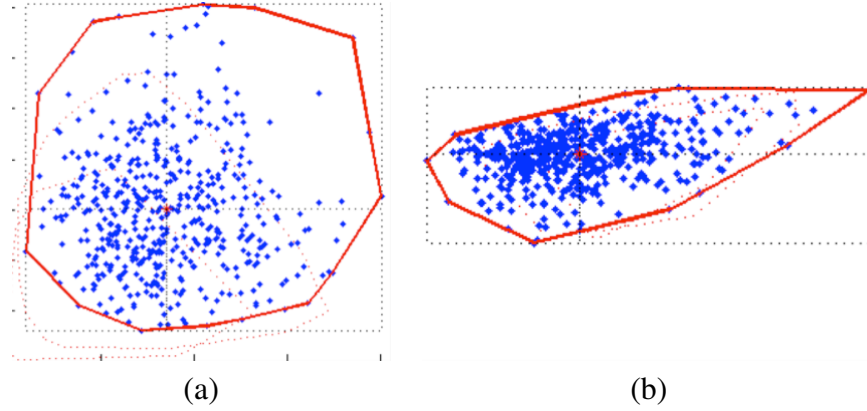


Figure 3.4: Illustration of the simulated dispersion of particles in the presence of two-dimensional perturbations over time. These noises are drawn according to a Weibull distribution, which has been shown to model surface current randomness. Depending on the distribution parameters, one can construct (a) a balanced, nearly isotropic dispersion pattern, or (b) a biased dispersion along a preferred dimension, to best model the ocean environment in the region of interest.

3.3.2 Search Strategy Comparison

The two search strategies to be investigated can be characterized as follows.

Linear Search

The searcher transits directly to the predicted location (based on time late, τ) of the drifting object under the influence of idealized flow with no random perturbations, and proceeds to execute a circular spiral out pattern for the duration, T , of the search mission. This naïve approach reflects current standard operating procedures for responding to a search cue, and as such, does not account for the ocean model-dependent expanding area nor the particle-based distribution information.

Myopic Search

The searcher uses the flow model with noise presented previously to predict the course of 500 simulated particles, recording the convex hull and centroid location information at each time step up through τ . Once the convex hull has been appropriately computed (which has $\mathcal{O}(n \log n)$ complexity in number of particles n), the searcher divides this area into four partitions along the direction of flow as well as in the orthogonal axis (as in Fig. 3.5). The number of particles in each of the four partitions is used to determine a prior probability of the object's likelihood to be in that partition. The searcher then can use the discrete myopic search algorithm described in Section 3.1.2 to allocate search effort in one-hour units up to search duration, T , among the four partitions. (We can assume the searcher employs an ideal search once in a partition.)

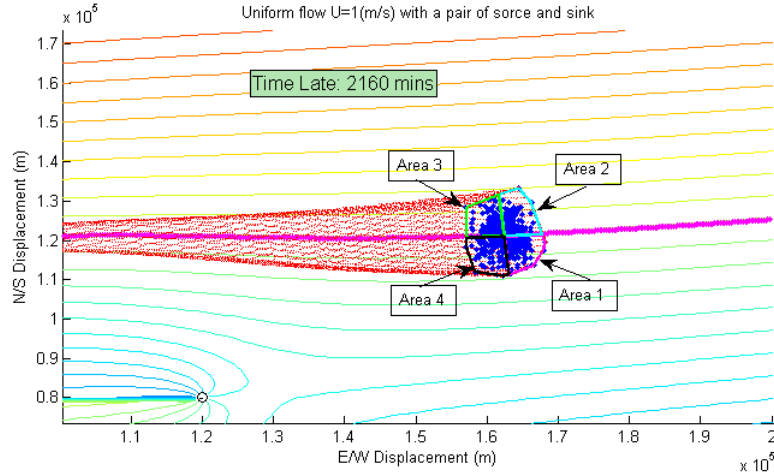


Figure 3.5: Simulation of a particle cloud is used to define a time-varying search area (i.e., the convex hull enclosing the particle cloud) as it evolves in time. The blue dots represent the locations of the 500 particles at a time late of 36 hours, and the red dotted outline shows the growing search area over each time interval. This area of uncertainty is then decomposed into four partitions, for each of which a prior probability of object presence is computed using the percentage of the total particles contained within.

Table 3.1: List of five factors used in the simulation runs to investigate their impact on search effectiveness

Factors	Typical Values	Description
Searcher speed (V) MQ8 Fire Scout	50.0 m/s ≈ 100 kts	Search speed of UAV
Drifter speed (U)	0.1 to 1.0 m/s	Min and max sea surface current speeds
Time Late (τ)	12 to 36 hrs	Time delay before Searcher can be on station
Search Time (T)	1 to 4 hrs	Amount of time Searcher has in area of interest
Sweep width (W)	100 to 1000 m	Nominal sensor performance

3.3.3 Relevant Factors and Design of Simulation Experiments

Though there may be numerous variables relevant to ocean and search models, the work presented in this thesis highlights a set of factors believed to be of operational concern for the search mission. These factors and their notional values are provided in Table 3.1.

We treat the initial location of the drifting object as an *uncontrollable factor* [34], and as such, the simulation code (written in Matlab) has been designed to enable such investigations of the

effect of arbitrary starting locations, as well as to incorporate other elements such as historical surface current data.

Given that each factor has a range of possible values, exhaustive examination of the factor space is not feasible, especially as the Monte Carlo nature of the particle cloud evolution imposes additional computational overhead. Overcoming this challenge is the essence of the field of statistical experimental design, where well-chosen combinations of factor values can be used to statistically infer the relationship between them and the response variable or the measure of performance [34]. For example, screening designs of experiments can use permutations of upper, lower and mean factor values to extract which factors, e.g., a subset of those listed in Table 3.1, are most significant in affecting the probability of detection. Numerical studies and their results for the simplified potential flow model highlighted in Section 3.2.2 as well as the studies and results based on the historical surface currents data obtained from the Shallow Water Assimilation Forecast System (SWAFS) are highlighted in the next chapter.

THIS PAGE INTENTIONALLY LEFT BLANK

CHAPTER 4:

Analysis of Model Output

In designing a simulation model, there is a need to ensure that the various building blocks are working in the right manner before we proceed to expand the analysis to include historic data sets, where a number of factors may make it difficult to troubleshoot where the model has gone wrong. The approach used in this thesis was to perform the search analysis with a simple potential flow model first, and then expand the analysis to include historic data sets obtained from SWAFS.

4.1 Search Analysis Using Potential Flow Model

During the search process, if the drifting object falls within the range of the searcher's sweep width, it is defined as a successful detection and the search is terminated and a value of one is assigned to the simulation run. If the searcher is unable to locate the object within the given search time, then a value of zero is assigned to the simulation run. The percentage of successful detections is obtained by counting the number of runs where the outcome of the simulation is set to one over the total number of simulation replications.

As described in Section 3.3, we chose a number of values from each factor for our simulation runs so as to infer the relationship between the search performance and the response variable. In addition, we note that the drifter speed is always proportional to the searcher speed and a better representation would be to indicate the drifter speed as a ratio of the searcher speed. That said, we fixed the searcher speed at 50 m/s for all our analysis and if we assume that the drifter is traveling at a constant speed of 1.0 m/s, we explain the analysis by saying that the drifter is moving at $U = 2\%$ of the searcher speed. Then, we chose the values listed in Table 4.1 and perform the simulation runs on 500 samples for both the linear search and myopic search strategies. Next, we repeat the entire simulation for a different start location of the drifter and verify if both sets of results are generally consistent. The total number of simulation runs completed for the potential flow model amounts to 144,000 simulation runs.

Though the data mining and analysis portion highlights various insights, we present the results for four analyses where the impact of the search and ocean model parameters on the probability of detection objective is evaluated. In the charts below, the horizontal axis denotes maximum

Table 4.1: List of values used in the simulation runs to investigate their impact on search effectiveness in the potential flow model for both myopic and linear search strategies

Factors	Values Used in Simulation
Drifter speed (U)	0.2%, 1% and 2% of V ; (0.1, 0.5 and 1.0 m/s)
Time Late (τ)	24 and 36 hrs
Search Time (T)	1, 2, 3 and 4 hrs
Sweep width (W)	100, 500 and 1,000 m

duration of the search mission, T , with the dependent axis representing the probability of detection (computed as the percentage of successful simulation trials). The search performance is shown for both search strategy types.

4.1.1 Analysis 1: Time Late, $\tau = 24$ hrs; Sweep Width, $W = 500$ m

Based on a time late of $\tau = 24$ hours, and a searcher with a sensor sweep width $W = 500$ meters, the simulation results for the case where the ratio of the object speed (based on current flow) to the searcher speed is $U = 2\%$ is shown in Fig. 4.1(a). The linear search approach continues to yield improved performance as the amount of time spent searching increases, whereas myopic search appears to plateau after two hours of search effort. This is because the drifting object has already moved out of the search zone within those two hours such that continued searching in subsequent areas is fruitless. We observe a crossover point where, although the myopic approach initially excels, linear search begins to perform better after a search duration time of about two hours.

For U at 1% (shown in Fig 4.1(b)) or less, both myopic and linear search have similar performance results that show detections occur nearly 100% of the trials. This fact shows that for small enough relative flow speeds, the expanding area does not increase too rapidly to be completely covered by a searcher with a sweep width of at least 500m.

4.1.2 Analysis 2: Time Late, $\tau = 24$ hrs; Sweep Width, $W = 100$ m

When the sensor sweep width is reduced from 500m to 100m, there is a sharp drop of about 60% in the detection probabilities for $U = 2\%$, as illustrated in Fig. 4.2(a). The same crossover is seen at search times near two hours, where linear search begins to outperform the myopic search with increasing T . On the other hand, once again, the performance of myopic search tapers off at about $T = 2$ hrs.

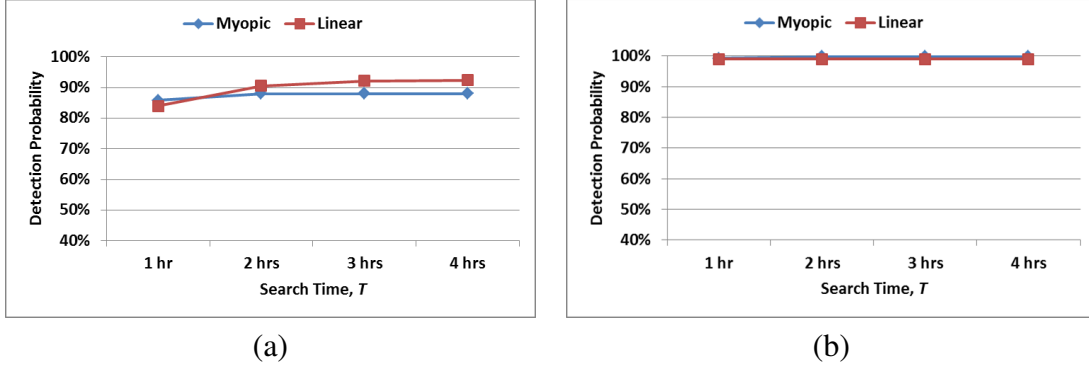


Figure 4.1: Probability of detections from simulation studies comparing linear search (red squares) and myopic search (blue diamonds). The search and ocean parameters are $\tau = 24$ hrs, $W = 500$ m, and object speed ratio is set to (a) $U = 2\%$, which sees linear search improving with increased search times, and (b) $U = 1\%$, where either search method yields nearly perfect detections due to the short time late and large sensor sweep width.

An interesting outcome is observed when U is reduced to 0.2% , shown in Fig. 4.2(b). There is a reversal in performance such that myopic search performs better when more than two hours are available for the search mission duration. For instance, myopic search achieves nearly 90% successful object detections at $T = 4$ hrs while linear search only manages an object detection rate of about 70% for the same duration. Further simulation studies for the range of U values show that this transition (between Fig. 4.2(a) and (b)) occurs when U is less than approximately 1% . Conversely, for faster surface currents, i.e., U approximately greater than 1% , linear search serves as the better search alternative, all other factors remaining constant.

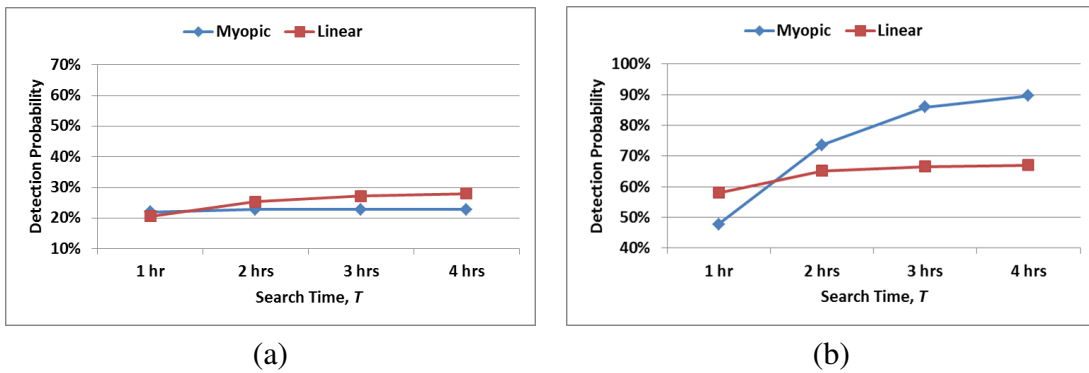


Figure 4.2: Search mission results for $\tau = 24$ hours, $W = 100$ m, and for (a) $U = 2\%$, and (b) $U = 0.2\%$. For shorter sensing distances and slower surface currents as in (b), the myopic search approach appears to vastly outperform the naïve linear search.

4.1.3 Analysis 3: Time Late, $\tau = 36$ hrs; Sweep Width, $W = 500$ m

Next, we investigate the impact of increased time late of $\tau = 36$ hours (with $W = 500$ m), which nominally only results in a larger search area due to further expansion over time as compared with the above analyses. In doing so, for surface current speed ratios $U = 2\%$ (depicted in Fig. 4.3(a)), linear search has about a 20% advantage in detecting the drifting object over myopic search as early as the first hour of search.

However, this advantage is quickly lost, as myopic search is able to produce similar search performances when search time allocated to the mission is increased to two hours or more as illustrated in Fig. 4.3(a). When U is reduced to 1%, as shown in Fig. 4.3(b), the most noticeable change is the diminished gap in performance (i.e., to only $\sim 10\%$) between the two search strategies at the one hour search mission mark. Note that thereafter, myopic search has a slightly better performance as compared to linear search.

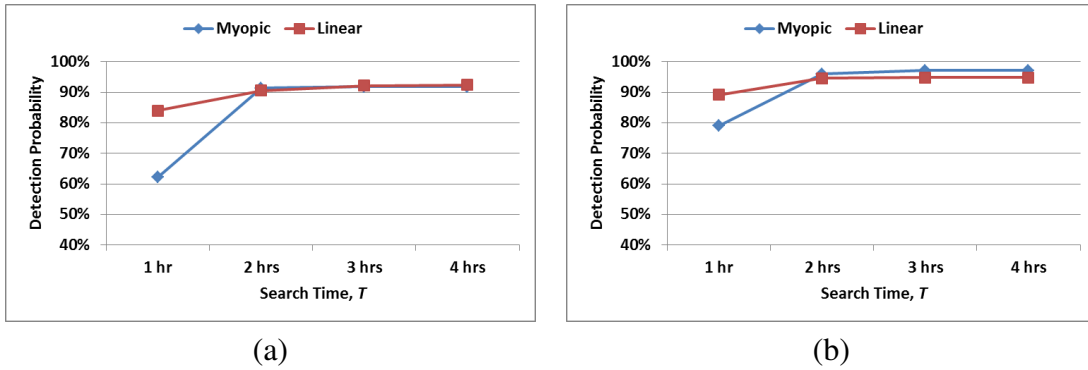


Figure 4.3: Search mission results for $\tau = 36$ hours, $W = 500$ m, and for (a) $U = 2\%$, and (b) $U = 1\%$. For faster surface speeds, the myopic search approach suffers initially by too narrowly focusing its search effort, although for both speed ratios, it appears to close the gap in search performance for missions extending past the initial first hour.

4.1.4 Analysis 4: Time Late, $\tau = 36$ hrs; Sweep Width, $W = 100$ m

As before, we examine what happens when the sensor sweep width is reduced to $W = 100$ m, for extended time late $\tau = 36$ hrs. As this is the most challenging operational case, we anticipate diminished search performance relative to the previous studies. As shown in Fig. 4.4(a) and (b), for $U = 2\%$ and $U = 0.2\%$, respectively, we observe that the highest probability of detection for either linear or myopic search strategies in the former analysis does not reach 30%, even with an extended search mission duration of four hours. This trend is similar to the chart shown in Fig. 4.2(a), which similarly had a short sensor range trying to search for faster-moving objects.

For slower surface currents, with $U = 0.2\%$, comparing the linear search performance between the shorter (e.g., Section 4.1.2) and longer time late values, detection probability drops by about 30% for search missions lasting a single hour, but only shows an 8% decrease in performance after four hours of search.

There is also a shift in the crossover point where myopic search begins to outperform linear search, as shown in Fig. 4.4(b). Compared to the previous analysis with $\tau = 24\text{hrs}$, now with a longer time late, this reversal occurs later at nearly four hours, highlighting the diminished advantage of using myopic search. The overall detection performance is also noticeably lower for this challenging scenario.

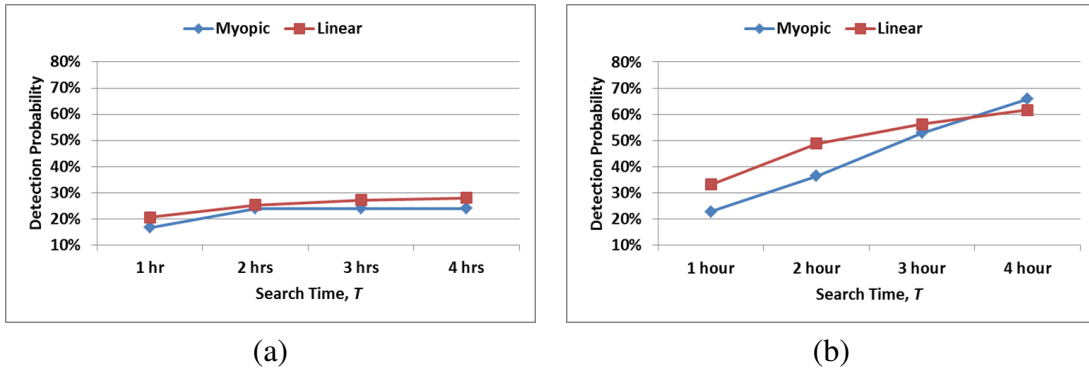


Figure 4.4: Search mission results for $\tau = 36$ hours, $W = 100\text{m}$, and for (a) $U = 2\%$, and (b) $U = 0.2\%$. Linear search appears to perform better than myopic search no matter the search mission duration when the drifting objects move relatively faster. For slow-moving objects, only after four hours does myopic search begin to perform marginally better.

4.1.5 Varying Initial Object Locations

Following the preliminary analysis for the target starting at a point above the generalized source-sink pair, the target was made to start its drift from another point that is located below the generalized source-sink pair (see Fig. 4.5). The outcome of the simulations demonstrated that the trends described in the previous sections appear to hold for arbitrary starting locations of the drifting object. These corroborating results further reinforce the relationships between these parameters described previously, and highlight the merit of further, more extensive sensitivity analyses.

4.2 Statistical Analysis on Potential Flow Model

Using the Student's T-test method, a hypothesis testing was carried out on the results. The null hypothesis, H_0 , is defined as “both myopic search and linear search have the same detection

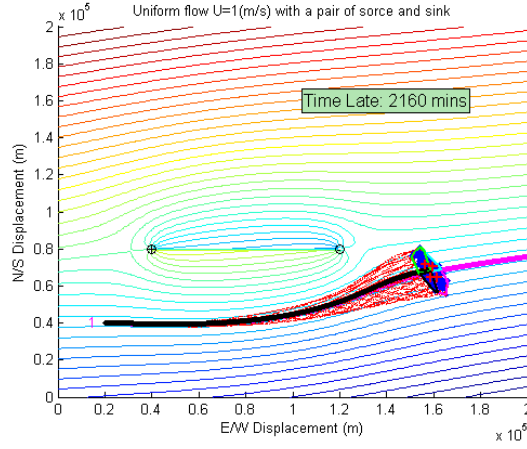


Figure 4.5: An example instance of an alternate initial location of the drifting object, such as below the source-sink pair. The functional dependencies of the probability of detection on the factors presented in this paper appear to hold for arbitrary initial locations.

performance” and the alternative hypothesis, denoted as H_1 , is that the “detection performance between myopic search and linear search are distinctively different.” For the result to be deemed significant, we chose the α -value to be 0.05 or 5%.

For sweep width (W) equal to 1000 m, we used the data analysis package in Microsoft Excel and performed a “T-test: Paired Two Sample for Means” on all the simulation results obtained from the various permutations of time late (τ), search time (T) and drifter speed (U). The calculated p -value of 0.74 is significantly greater than α and thus we do not reject the null hypothesis (i.e., there is no evidence to infer that the alternative hypothesis is true). Next, we repeat the data analysis for $W = 500$ m. The calculated p -value was 0.0318, which is deemed significant as it lies between 0.01 and 0.05. Given that the p -value is less than α , there is strong evidence to infer that the alternative hypothesis is true and we reject the null hypothesis (i.e., the detection performance between myopic search and linear search are likely to be different). As expected, when W is reduced further to 100 m, the calculated p -value was 0.0029, which is highly significant and provides overwhelming evidence to infer that the alternative hypothesis is true.

The statistical analysis showed that, given a large W , the search performance between the two strategies will likely yield the same results. That is because the area created by the convex hull of the 500 samples is relatively small as compared to the area that can be covered by the searcher with a large W of 1000 m. Intuitively, the ratio between the two areas starts to increase if W is reduced by 50% to 500 m or 90% to 100 m and we are able to note a distinct difference

in detection probability results between linear search and myopic search.

Fig. 4.6(a) shows the comparison of the mean detection probability and standard error for both myopic and linear search. For $W = 1000$ m, the mean and standard error obtained for myopic search is 99.19% and 0.29%, respectively. For linear search, the mean was 99.1% and a standard error of 0.15%. For $W = 500$ m, myopic search achieved a mean of 94.03% with a standard error of 1.15%, while linear search has a slightly higher mean of 95.43% and a standard error of 0.68%. For $W = 100$ m, the mean detection probability for myopic search was 38.8% with a standard error of 2.98%, while linear search continues to fare better with a higher mean of 43.08% and a standard error of 2.33%. Notwithstanding, we note that there is a consistent sharp drop in detection probability when W is reduced from 500 m to 100 m, as shown in Fig. 4.6(b). This observation highlights the possibility of a non-linear relationship between detection probability and the linear decrease of sweep width. As such, additional values of W , spreading across 500 m to 100 m, needs to be investigated. Another interesting analysis is that the graphs in Fig. 4.6 showed that the naïve linear search starts to outperform the myopic search for shorter sensing distances.

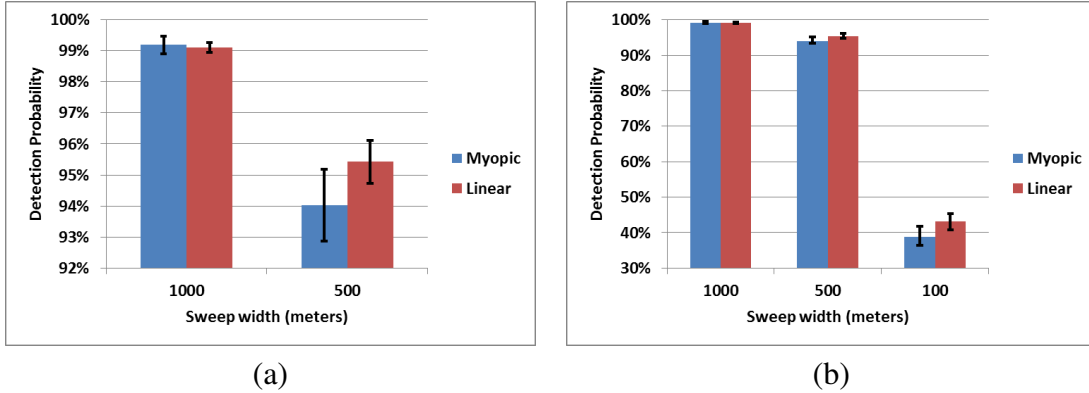


Figure 4.6: Comparison of the mean probability of detection between myopic search and linear search for W of 1000 m, 500 m and 100 m

4.3 Search Analysis Using Historical Data Set

Historical data sets obtained from SWAFS provide the surface current speeds ($water_u$ and $water_v$ variables) at hourly intervals for the months of March to August 2006. The hourly surface current data are spread out on a grid of 452 x 404 points covering the entire Persian Gulf region from 23.48°N, 47.49°E to 30.5°N, 57.51°E. For this thesis, we focused the simulation work and analysis primarily on the northern Persian Gulf region (28.5°N, 48°E to 30°N, 50°E) in order to draw references from the study done by Williams in 2007 on the High/Low wind

events during summer and winter. Similar to the potential flow model discussed in the earlier section, we chose two different start locations for the drifter as plotted in Fig. 4.7. Drifter start location 1 is about 100 km offshore from the nearest land mass on the west, while location 2 is chosen to be about 30 km away from the northern land mass. The resultant separation of the two locations is approximately 88 km and the a priori understanding is that the effects of LSBC and tides should have a more pronounced effect at location 2 as compared to location 1, thereby generating stronger surface current speeds.

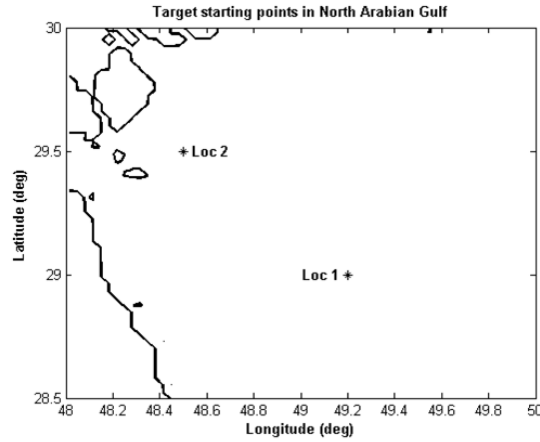


Figure 4.7: Drifter starting locations in north Persian Gulf. Location 1 is situated at 29°N, 49.2°E while location 2 is at 29.5°N, 48.5°E

Using the 2D interpolation method in Matlab, the surface current speed and angle are calculated and the drifter position is recorded at intervals of five minutes. So, for $\tau = 24$ hours, there are a total of 288 data point calculations to show the drifter movement. This process is performed for drifters starting at location 1 and 2 as well as for the two dates chosen (i.e., 15 April and 15 July) in this analysis. The mean wind speed on 15 April is less than 5 m/s, whereas the mean wind speed on 15 July is higher than 5 m/s. Fig. 4.8 shows the drifter plots, without noise added, for $\tau = 24$ hours. While the quiver plot snapshots taken at the end of 24 hours for all four plots do point to the fact that surface current flows for both locations are generally in the same direction (i.e., on 15 April, the surface current speed is flowing towards northwest while on 15 July, the flow is to the east), the drifter plots showed that there is a distinct difference between the surface currents affecting the drifter movement at location 1 as compared to location 2, with location 2 registering a higher mean target speed.

The plot of the drifter positions found in Fig. 4.8 also portrayed the fluctuations in surface currents due to variations in tides and wind direction over a period of 24 hours. Taking an

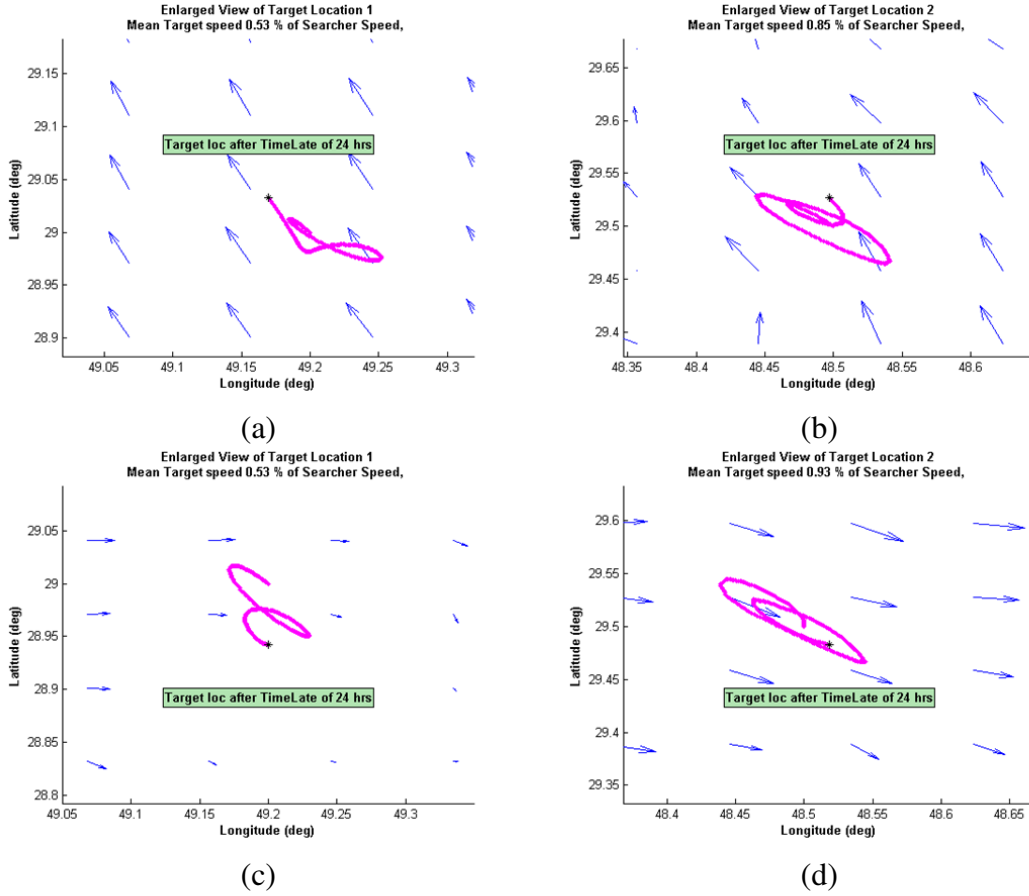


Figure 4.8: Drifter plots, without noise, for $\tau = 24$ hours, on 15 April for (a) location 1, and (b) location 2, as well as on 15 July for (c) location 1 and (d) location 2. The magenta line represents the drifter movement and the * symbol is used to denote the final position of the drifter at the end of 24 hrs.

hourly snapshot of the surface currents on 15 April, we found that at about $\tau = 4$ hrs, the surface current flow in the northern Persian Gulf started to move southeast along the major axis with an intensification of the flow at around $\tau = 6$ to 8 hrs before subsiding at $\tau = 10$ hrs and finally reversing the flow towards northwest at about $\tau = 12$ hrs (See Fig. 4.9 (a) to (f)). This flow pattern is repeated at semidiurnal periods with the same flow towards northwest at about $\tau = 24$ and 36 hrs (See Fig. 4.10 (a) and (b) respectively), suggesting that the dominant driver of the surface current speed on the 15 April is due to tidal currents.

To illustrate the drifter speed, we determined the mean speed that the drifter was traveling and presented it as a percentage of searcher speed. For example, in Fig. 4.8(a) the mean target speed at location 1 on 15 April was 0.53% of searcher speed or in other words, with a searcher speed of 50 m/s, the target was traveling at an average speed of 0.265 m/s. That also means

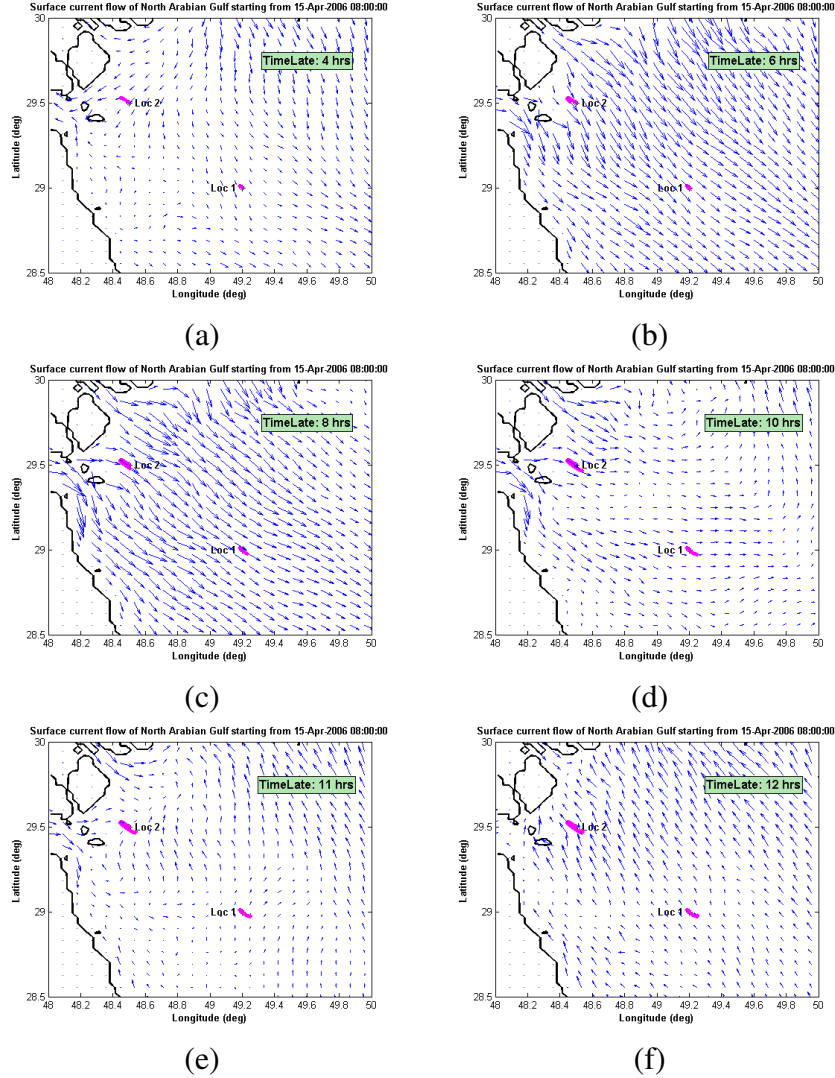


Figure 4.9: Surface current flow on 15 April, for (a) $\tau = 4$ hrs, (b) $\tau = 6$ hrs, (c) $\tau = 8$ hrs, (d) $\tau = 10$ hrs, (e) $\tau = 11$ hrs and (f) $\tau = 12$ hrs. Surface currents tend to flow towards the northwest at semidiurnal periods

that the distance traveled by the drifter over a duration of 24 hours was 22,896 m. However, this value should not be interpreted as saying the drifter is now approximately 22 km away from where it first started. By inspecting the plots in Fig. 4.8, we are able to discern that the distance separating the start and final position of the drifter is actually much less than the distance traveled based on mean speed calculations. As such, if we had used the mean speed value and the mean direction of travel to plot the drifter position, it would result in a large error (as shown in Fig. 4.11) between the exact drifter position and the calculated mean position.

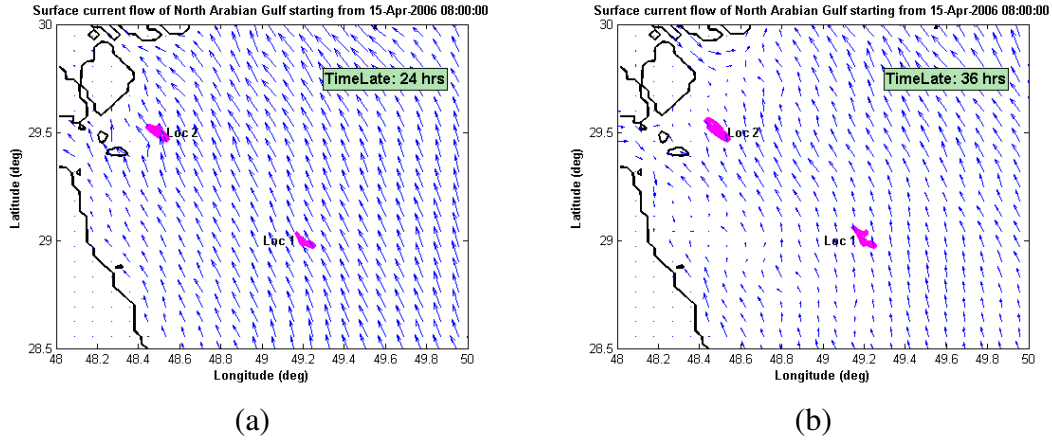


Figure 4.10: Surface current flowing northwest on 15 April, for (a) $\tau = 24$ hrs and (b) $\tau = 36$ hrs

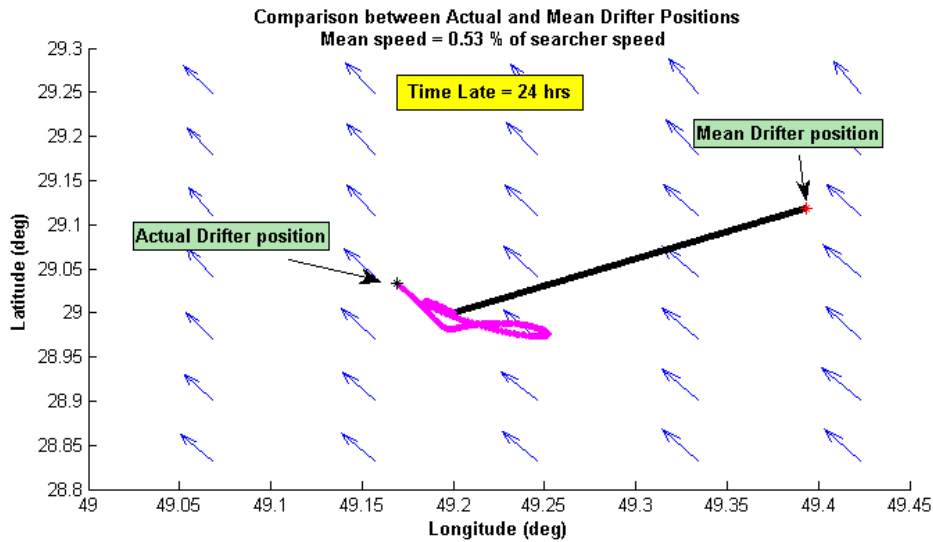


Figure 4.11: Illustration of the difference between using the mean speed (0.53% or 0.265 m/s) and direction (035°) to plot the drifter position in time as compared to using the interpolated speed and direction of the surface currents calculated at five-minute intervals.

With the U speed being defined by the historical data set, the same factors and values that was used in the potential flow model was chosen for the simulation runs. One of the findings from the potential flow model was that there exists a possible non-linear drop in detection probability when W is reduced from 500 m to 100 m and greater resolution of W was needed. Assuming a linear drop in detection probability, we added additional values of W (i.e., 600 m, 400 m, 300 m and 200 m) that are spaced 100 m apart. Subsequent analysis showed that the steepest gradient occurred when W was reduced from 200 m and 100 m. As such, three additional values of W spaced 25 m apart were introduced into the simulation runs, resulting in a total of ten different

Table 4.2: List of factor values that are used in the simulation runs with drifter speed, U , being extracted from the historical data set provided by SWAFS.

Factors	Values Used in Simulation
Time Late (τ)	24 and 36 hrs
Search Time (T)	1, 2, 3 and 4 hrs
Sweep width (W)	100, 125, 150, 175, 200, 300, 400, 500, 600 and 1000 m

values of W investigated with a total of 320,000 simulation runs conducted. Table 4.2 lists the different factor values that were investigated with the historical data set.

As explained in Section 3.2.3, we introduced Weibull-distributed perturbations to the drifter paths at each time step to create random dispersions of the drifter cloud. The enclosing convex hull (i.e., formed by the dotted red line) shown in Fig. 4.12 thus correspond to the 3σ expanding uncertainty area created by the 500 simulated particles. Thereafter, linear search and myopic search strategies (See Section 3.3.2) were performed on all 500 particles and the search results tabulated and expressed as a percentage of the total detection probability. Shown in Fig. 4.12 are the search results for particle number 1 at varying sweep widths of 1,000 m, 500 m, 200 m and 100 m. In essence, the searcher is able to locate particle number 1 in all four illustrations but the time taken to conduct the search increases as W is reduced. If the search time, T , is limited to only the 1st hour, then the searcher is only able to locate the target if it uses a sensor with a sweep width of 1,000 m. Similarly, if T is increased to 2 hours, the minimum W setting must be set at 500 m in order to localize the target within the allocated search time.

Another point to note and is also shown in Fig. 4.12(a) and (b) is that for $W \geq 500$ m, they will have the same Search Plan (i.e., [1, 3, 2, 4]). That is to say, the searcher will proceed to conduct its search operations in area 1 for the 1st hour, area 3 for the 2nd hour, area 2 for the 3rd hour and finally, area 4 at the 4th hour. However, when W is reduced to less than or equal to 200 m, there is a shift in the order of the Search Plan with area 4 being assigned as the area to search for the 2nd hour, area 3 to be searched in the 3rd hour and area 2 to be searched in the 4th hour. This shift in search plan is a result of the “greedy” algorithm in myopic search technique as described in Section 3.1.2. With the reduction in sweep width, the searcher can no longer fully cover the entire area of uncertainty within the user-defined search duration of 1 hour and thus needs to adopt a locally optimal plan that will maximize the chances of detecting the drifter while minimizing the mean time it takes to do it.

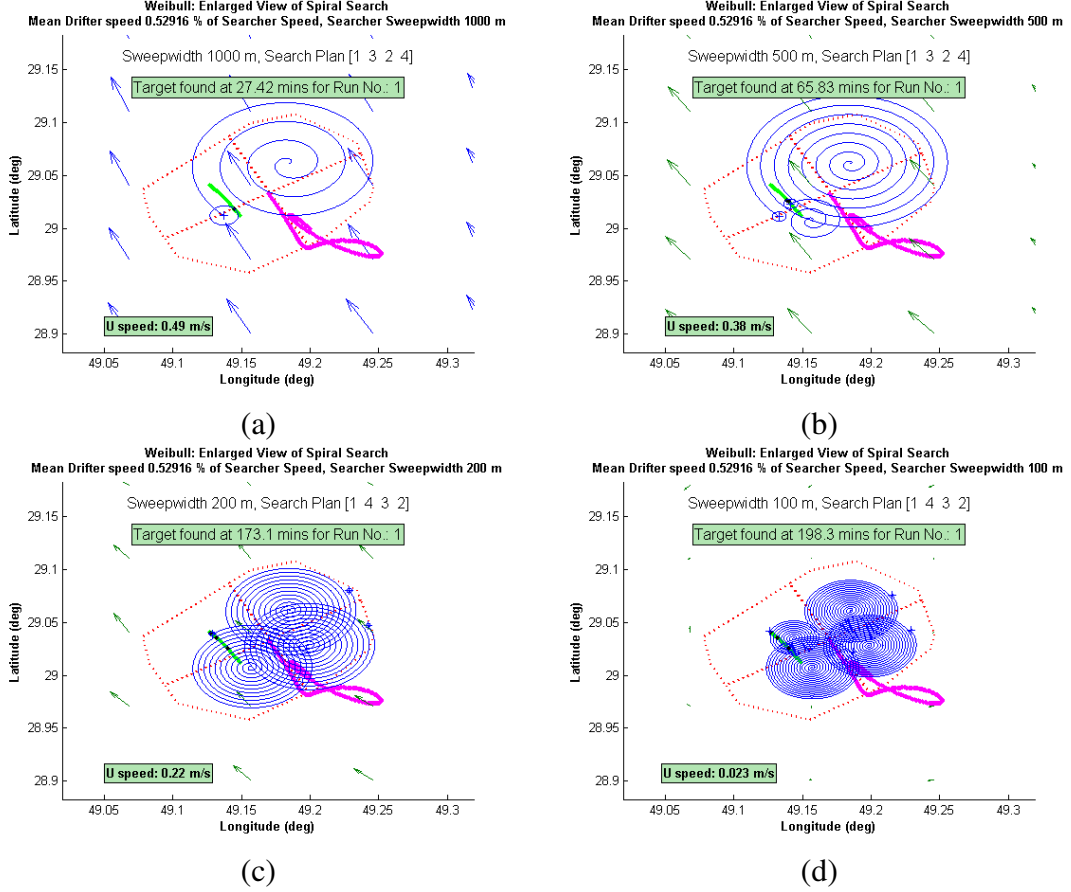


Figure 4.12: Search results for particle run number 1 starting at location 1 on 15 April for $\tau = 24$ hrs with a variation of W ((a)1000 m, (b)500 m, (c)200 m and (d)100 m) being evaluated. As W reduces, the "greedy" algorithm recommends an alternative search plan that maximizes the detection probability while minimizing the search cost (i.e., time)

Next, we present the results for 12 cases where the impact of the search and ocean model parameters on the probability of detection is evaluated. Cases 1 to 4 looked at the differences in detection probability between location 1 and 2 on 15 April 2006 when different values of time late (i.e., 24 and 36 hours) and sweep width (i.e., 500 and 100 m) are used. Similarly, cases 5 to 8 looked at the results obtained on 15 July 2006 with the same permutations of time late and sweep width. Finally, cases 9 to 12 focused on the change in the detection probability curves for the entire sweep width range (i.e., 1,000 m to 100 m) as well as different values of time late for each location on 15 April. A summary of the different values used in each case is illustrated in Table 4.3.

Table 4.3: List of 12 cases and their associated parameters used in the simulation runs based on the historical data set.

Case	Date	Time late (hrs)	Sweep width (m)	Remarks
1	15 Apr	24	500	Comparing the difference in detection probability between location 1 and 2
2	15 Apr	36	100	
3	15 Apr	24	500	
4	15 Apr	36	100	
5	15 Jul	24	500	
6	15 Jul	36	100	
7	15 Jul	24	500	
8	15 Jul	36	100	
9	15 Apr	24	1,000 to 100	Detection probability curves at location 1
10	15 Apr	36	1,000 to 100	
11	15 Apr	24	1,000 to 100	Detection probability curves at location 2
12	15 Apr	36	1,000 to 100	

4.3.1 Case 1: 15 April, Time Late, $\tau = 24$ hrs; Sweep Width, $W = 500$ m

Based on a time late of $\tau = 24$ hours, and a searcher with a sensor sweep width $W = 500$ meters, the simulation results for the case where the drifter was dropped at location 1 on 15 April is shown in Fig. 4.13(a), whereas Fig. 4.13(b) shows the results where the drifter was dropped at location 2. The mean speed at location 1 was 0.265 m/s (0.53% of searcher speed, V) while the mean speed at location 2 was 0.425m/s (0.85% of V). The linear search approach continued to perform better than myopic search during the first search hour and appeared to plateau after two hours of search effort. This is because the drifting object had already moved out of the search zone within those two hours such that continued searching in subsequent areas was fruitless. We observed a crossover point where, although the linear search approach initially excelled, myopic search began to perform slightly better after search duration time of about two hours.

While the drifter at location 2 was experiencing a mean speed that was 60% more than location 1, the simulation results showed that it has relatively little impact when the searcher is using a sweep width of at least 500m. This fact again reemphasized the earlier point as proven in the potential flow model that, for small enough relative flow speeds, the expanding area does not increase too rapidly to be completely covered by a searcher with a sweep width of at least 500m.

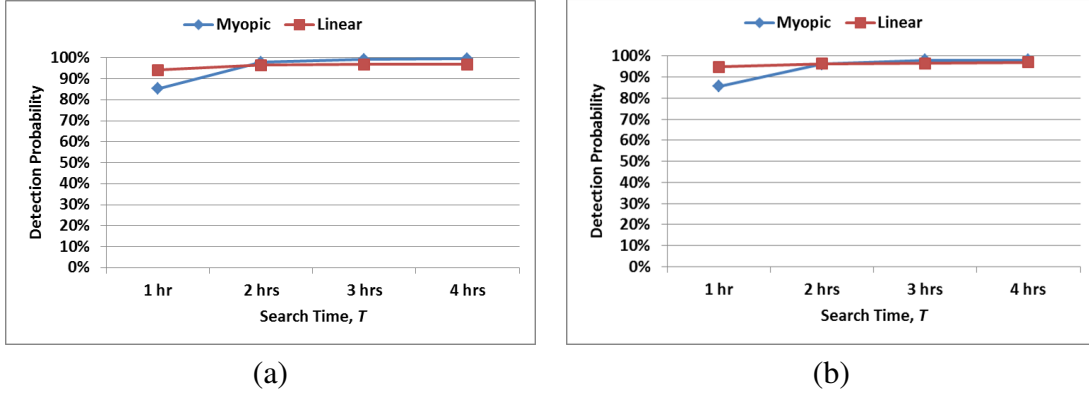


Figure 4.13: Probability of detections from simulation studies comparing linear search (red squares) and myopic search (blue diamonds). The search and ocean parameters are $\tau = 24$ hours, $W=500$ m, and mean surface current speed or object speed ratio at location 1 (a) $U=0.265\text{m/s}$ (0.53% of V) and at location 2, (b) $U=0.425\text{m/s}$ (0.85% of V). For both cases, there is a crossover point at $T = 2\text{hrs}$ where myopic search performs slightly better than linear search

4.3.2 Case 2: 15 April, Time Late, $\tau = 24$ hrs; Sweep Width, $W = 100$ m

When the sensor sweep width was reduced from 500m to 100m, there was a sharp drop of about 60% in the detection probabilities for linear search in both location 1 and 2. Myopic search also suffered from approximately 60% drop in location 1 and about 70% drop in detection probability in location 2. As illustrated in Fig. 4.14(a), with a slower mean surface current speed of 0.265m/s, there was a crossover seen only after search time, T , of four hours where myopic search began to outperform the linear search. However, when the mean surface speed was increased by 60% in location 2, there was no such crossover observed and linear search outperformed myopic search for all values of T (See Fig. 4.14(b)).

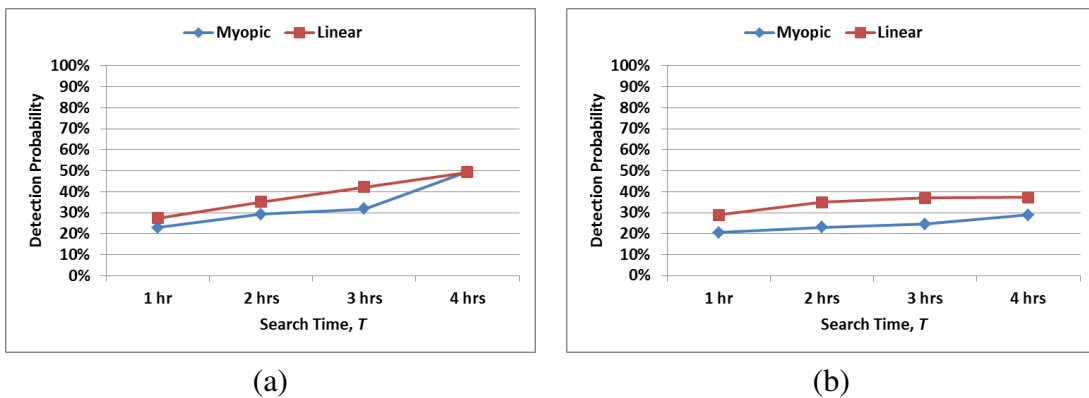


Figure 4.14: Search mission results for $\tau = 24$ hours, $W = 100$ m, and for mean surface current speed or object speed ratio at location 1 (a) $U=0.265\text{m/s}$ (0.53% of V) and at location 2, (b) $U=0.425\text{m/s}$ (0.85% of V). For shorter sensing distances and slower surface currents as in (a), the myopic search approach appears to only outperform the naïve linear search at $T = 4$ hours

4.3.3 Case 3: 15 April, Time Late, $\tau = 36$ hrs; Sweep Width, $W = 500$ m

As with the potential flow model, we next investigated the impact of increased time late of $\tau = 36$ hours (with $W = 500$ m), which nominally only results in a larger search area due to further expansion over time as compared with the above cases. The overall mean surface current speed increased by about 3% for location 1 to 0.2725 m/s (0.545% of V) and about 1.5% for location 2 to a mean speed of 0.4315 m/s (0.863% of V).

In doing so, we observed that there was approximately 15% and 6% drop in detection probability for myopic search and linear search respectively, when we compared the results for location 1 and 2 at $T = 1$ hour with the results in Section 4.3.1. However, this disadvantage was quickly regained, as both myopic search and linear search was able to produce similar search performances as in Section 4.3.1, when search time allocated to the mission was increased to two hours or more as illustrated in Fig. 4.15(a) and (b). What this means is that while the expanding search area may have grown bigger with $\tau = 36$ hours, it had twice the impact on myopic search than linear search. However, this degradation was only limited to $T = 1$ hour, as both search techniques were able to close the performance gap for missions extending past the first hour. In addition, the 58% difference in U between location 1 and 2 did not affect the overall performance of the mission between the two search techniques past the first hour.

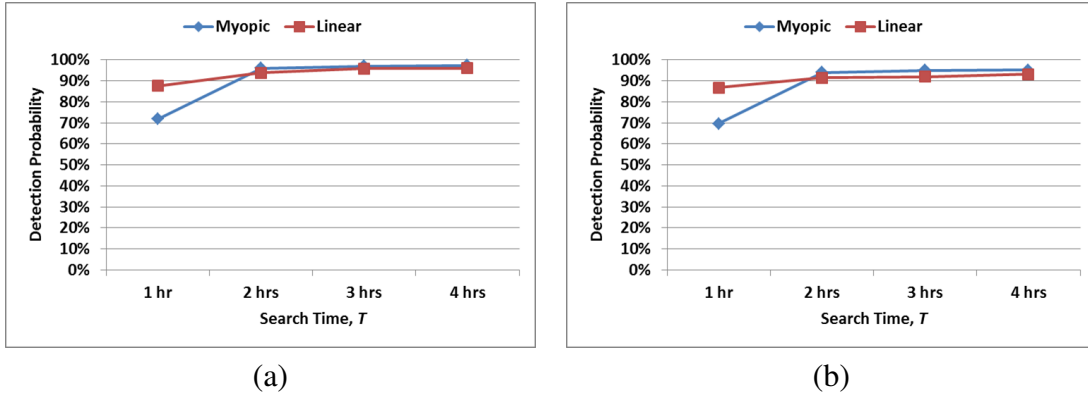


Figure 4.15: Search mission results for $\tau = 36$ hours, $W = 500$ m, and for mean surface current speed at location 1 (a) $U = 0.2725$ m/s (0.545% of V) and at location 2, (b) $U = 0.4315$ m/s (0.863% of V). For larger search area, myopic suffered more initially but managed to regain its performance past the initial hour. The 58% difference in U had minimal impact on search performance

4.3.4 Case 4: 15 April, Time Late, $\tau = 36$ hrs; Sweep Width, $W = 100$ m

As before, we examined what happened when the sensor sweep width was reduced to $W = 100$ m, for extended time late $\tau = 36$ hrs. Relative to previous studies, we anticipated diminished search performance. As shown in Fig. 4.16 (a) and (b), for $U = 0.2725$ m/s (0.545% of V) and

$U = 0.4315\text{m/s}$ (0.863% of V), respectively, we observed that there was about 17% drop in the highest probability of detection for myopic search when compared with the former case, even with an extended search mission duration of four hours. Linear search fared much better with only about 10% drop in the highest probability of detection when compared with the former case. Linear search also continued to outperform myopic search for all search times, as shown in Fig. 4.16 (a) and (b).

Given that location 2 had a 58% increase in U , the overall detection performance was expected to be lower as compared to location 1. From Fig. 4.16, there was an approximately 10% difference in search performance at the extended search duration of four hours for myopic search and about 6% for linear search when comparing the results between (a) and (b).

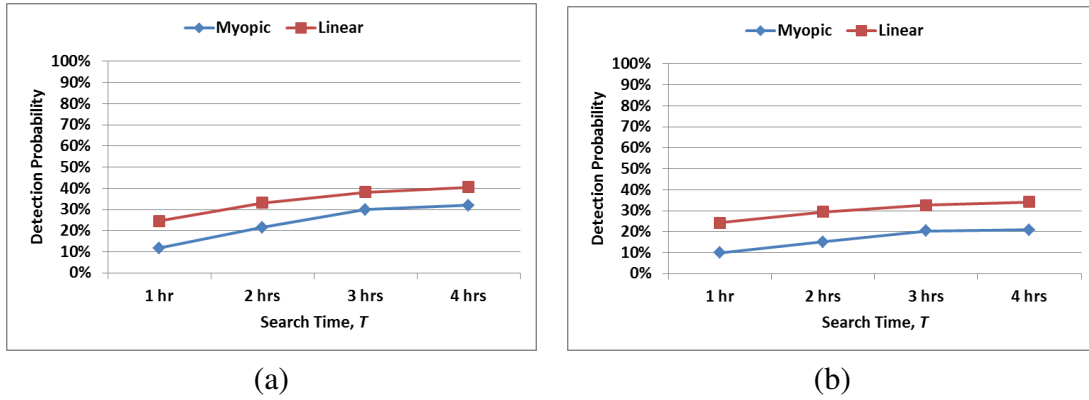


Figure 4.16: Search mission results for $\tau = 36$ hours, $W = 500$ m, and for mean surface current speed at location 1 (a) $U = 0.2725\text{m/s}$ (0.545% of V) and at location 2, (b) $U = 0.4315\text{m/s}$ (0.863% of V). Linear search outperformed myopic search regardless of the search mission duration and mean U speed

4.3.5 Case 5: 15 July, Time Late, $\tau = 24$ hrs; Sweep Width, $W = 500$ m

Next, we looked at the surface current conditions on 15 July where the mean wind speed data points was above 5m/s. Based on a time late of $\tau = 24$ hours, and a searcher with a sensor sweep width $W = 500$ meters, the simulation results for the case where the drifter was dropped at location 1 and location 2 on 15 July is shown in Fig. 4.17(a) and (b) respectively. The mean speed at location 1 was 0.265 m/s (0.53% of searcher speed, V) while the mean speed at location 2 was 0.463m/s (0.926% of V). That is to say, location 2 experienced a mean surface current speed that was 75% more than location 1.

Linear search continued to perform better than myopic search during the first search hour and appeared to plateau after two hours of search effort because the drifting object had already

moved out of the search zone within those two hours. We observed a crossover point where myopic search began to perform slightly better after search duration time of about two hours. Similar to Section 4.3.1, while the drifter at location 2 was experiencing a mean speed that was 75% more than location 1, the simulation results showed that it had relatively little impact for $\tau = 24$ hours and when the searcher was using a sweep width of at least 500m. The expanding area did not increase too rapidly and could easily be completely covered by a searcher with a sweep width of at least 500m.

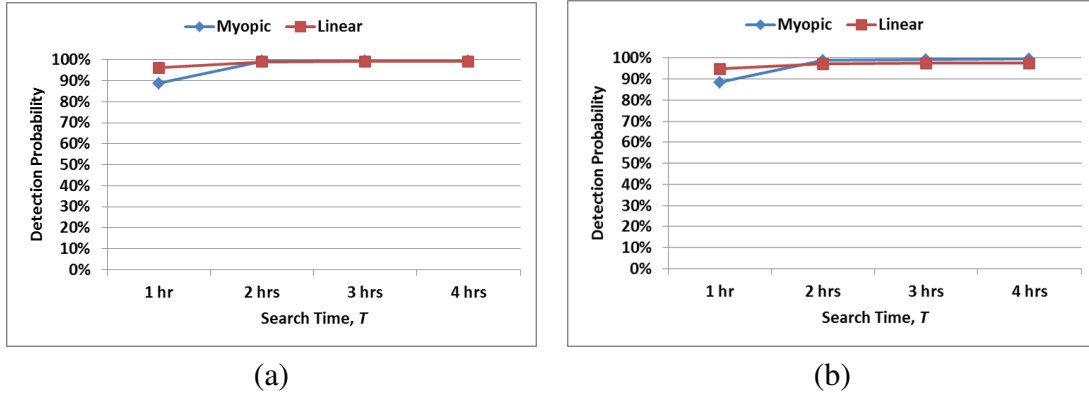


Figure 4.17: Probability of detections from simulation studies carried on two locations on 15 July. The search and ocean parameters were $\tau = 24$ hours, $W=500$ m, and mean surface current speed or object speed ratio at location 1 (a) $U=0.265\text{m/s}$ (0.53% of V) and at location 2, (b) $U=0.463\text{m/s}$ (0.926% of V). For both cases, there was a crossover point at $T = 2\text{hrs}$ where myopic search performed slightly better than linear search

4.3.6 Case 6: 15 July, Time Late, $\tau = 24$ hrs; Sweep Width, $W = 100$ m

When the sensor sweep width was reduced from 500m to 100m, linear search experienced a drop of about 60% in detection probabilities for the first hour of search in both location 1 and 2. Myopic search, however, suffered from an average of about 65% drop in detection probabilities in location 1 and 2 during the first search hour. For both locations, there existed a crossover point after search time, T , of 3 hours where myopic search started to outperform linear search by about 10 to 12% at the extended search duration of four hours. Next, we compared the impact of the 75% increase in mean surface speed at location 2. We observed that there was a slight reduction of about 6% in detection probability, as shown in Fig. 4.18, for both myopic and linear search at the extended search duration of four hours.

4.3.7 Case 7: 15 July, Time Late, $\tau = 36$ hrs; Sweep Width, $W = 500$ m

We continued the same analysis and investigated the impact of increased time late of $\tau = 36$ hours (with $W = 500$ m). The overall mean surface current speed decreased by about 4% for

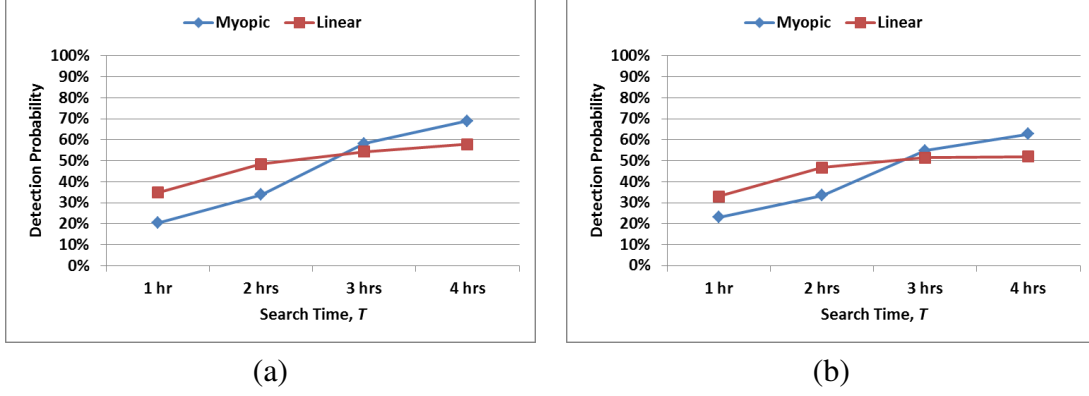


Figure 4.18: Search mission results for $\tau = 24$ hours, $W = 100$ m, and for mean surface current speed or object speed ratio at location 1 (a) $U = 0.265 \text{ m/s}$ (0.53% of V) and at location 2, (b) $U = 0.463 \text{ m/s}$ (0.926% of V). Myopic search approach appeared to only outperform the naïve linear search at $T = 3$ hours

both locations 1 and 2. The mean surface current speed at location 1 is now 0.255 m/s (0.51% of V) while location 2 is experiencing a mean speed of 0.443 m/s (0.885% of V).

With a larger search area due to the increased time late, we observed that myopic search experienced a drop in detection probability of about 16% and 18% at location 1 and location 2 respectively, when we compared the results for location 1 and 2 at $T = 1$ hour with the results in Section 4.3.5. Similarly, linear search also suffered a drop in detection probability of about 8% for both locations during the first hour of search. As such, the expanding search area with $\tau = 36$ hours has twice the impact on myopic search than linear search.

When the search mission was extended to two hours or more as illustrated in Fig. 4.19, both myopic search and linear search were able to achieve comparable search performance with an average of about 98% in detection probability. In addition, the 74% difference in U between location 1 in Fig. 4.19(a) and location 2 in Fig. 4.19(b) only affected the overall performance of the two search strategies by a maximum reduction of 4% during the first search hour. The impact of the increased U was subsequently reduced to a maximum of about 1.6% when the mission was extended to four hours.

4.3.8 Case 8: 15 July, Time Late, $\tau = 36$ hrs; Sweep Width, $W = 100$ m

Next, with the sensor sweep width reduced to $W = 100$ m and for extended time late $\tau = 36$ hrs, we expected a diminished search performance. Fig. 4.20(a) and (b) show the simulation results for location 1, with $U = 0.255 \text{ m/s}$ (0.51% of V) and location 2, with $U = 0.443 \text{ m/s}$ (0.885% of V), respectively. When compared with the simulation results in Section 4.3.6, we observed that

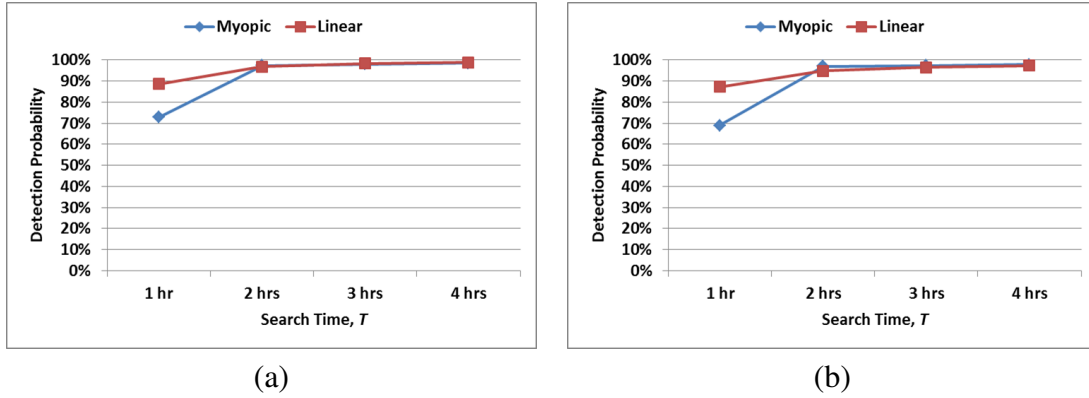


Figure 4.19: Search mission results for $\tau = 36$ hours, $W = 500$ m, and for mean surface current speed at location 1 (a) $U=0.255\text{m/s}$ (0.51% of V) and at location 2, (b) $U=0.443\text{m/s}$ (0.885% of V). Myopic suffered more initially but managed to regain its performance past the initial hour. The 74% increase in U had minimal impact on the search performance

there was about 13% drop in the highest probability of detection for myopic search for search mission duration of four hours.

Linear search fared much better, with only about 2% to 5% drop in the highest probability of detection. Linear search also continued to outperform myopic search for search times less than or equal to three hours, as shown in Fig. 4.20(a) and (b). In addition, there existed a crossover point for both locations where, after a search time of four hours, myopic search began to perform slightly better than linear search. While location 2 had a 74% increase in U , the overall detection performance between Fig. 4.20(a) and (b) was about 5% difference in search performance at the extended search duration of four hours for both myopic search and linear search.

4.3.9 Case 9: 15 April, Location 1, Time Late, $\tau = 24$ hrs; Search Time, $T = 1$ to 4 hours

Earlier simulations results from the potential flow model indicated the possibility of a non-linear relationship between sweep width and detection probability. However, as there were only three settings of sweep width (i.e., 100, 500 and 1,000 m) used in the potential flow model, it was difficult to discern if the relationship between sweep width and detection probability was linear or otherwise. As such, we added a total of seven more sweep width settings into our simulation runs as shown in Table 4.2 and the simulation results showed that the detection probability for both linear and myopic search strategies decreased non-linearly with sweep width, with the sharpest drop in the detection probability of about 30% to 40% between 200 m and 100 m.

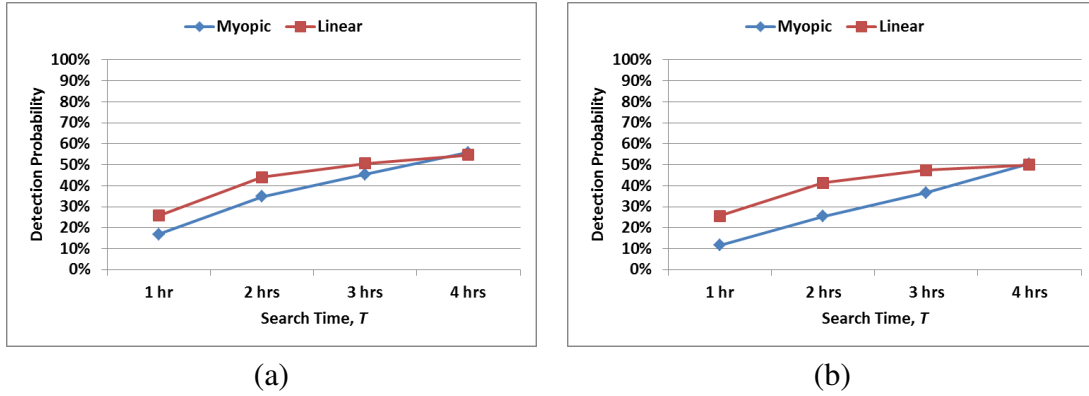


Figure 4.20: Search mission results for $\tau = 36$ hours, $W = 500$ m, and for mean surface current speed at location 1 (a) $U = 0.255$ m/s (0.51% of V) and at location 2, (b) $U = 0.443$ m/s (0.885% of V). Linear search outperformed myopic search for search mission duration less than or equal to 3 hours. Myopic search only managed to perform slightly better when the search duration was extended to four hours. The 74% increase in U caused a 5% drop in detection probability

Further analysis in Section 4.4 will provide an explanation of the cause of this non-linearity relationship.

For now, we focused the analysis on the positive impact of extending mission search time, T , as well as the response between myopic and linear search on increasing T . As shown in Fig. 4.21(a), for $T = 1$ hour, we observed that linear search performed better for all ranges of sweep width. When T was increased to two hours, myopic search was able to achieve comparable search performance and performed slightly better than linear search when the sweep width is more than or equal to 400 m. There existed a crossover point at W between 400 and 300 m as shown in Fig. 4.21(b), where linear search performed better than myopic search. Similar detection probability curves were observed for $T = 3$ hours and 4 hours as illustrated in Fig. 4.21(c) and (d). We observed that the crossover point where linear search started to perform better was progressively shifted towards a sweep width of 300 m as the search duration was increased further. By extending the mission search time to four hours, we also observed an approximately 10% increase in detection probability when W was set at 100 m.

4.3.10 Case 10: 15 April, Location 1, Time Late, $\tau = 36$ hrs; Search Time, $T = 1$ to 4 hours

When τ was increased to 36 hours, we noted from our earlier analysis that the increase in search area uncertainty would lead to a reduction of detection probability. The drop in detection probability was more pronounced for myopic search when the search duration was set at 1

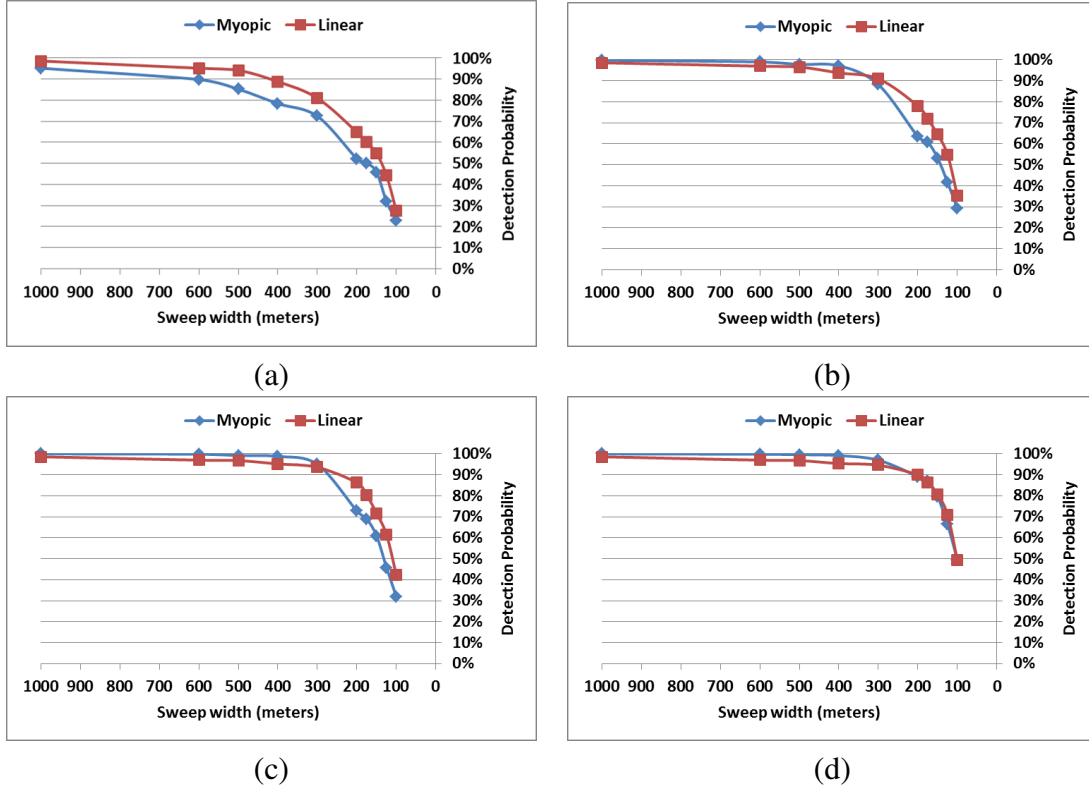


Figure 4.21: Search mission results at location 1 for $\tau = 24$ hours, W ranging from 100 m to 1,000 m, and for varying search time with (a) $T = 1$ hour, (b) $T = 2$ hours, (c) $T = 3$ hours and (d) $T = 4$ hours. Linear search outperformed myopic search for all sweep width settings at search mission duration equal to 1 hour with myopic search performing better at $W \geq 400$ m for extended durations. The crossover point where linear search performed better was observed to progressively shift towards W of 300 m when T increased

hour as shown in Fig. 4.22(a). When T was increased to two hours, linear search continued to perform better than myopic search at W between 400 and 300 m as shown in Fig. 4.22(b). Similar detection probability curves were observed for $T = 3$ hours and 4 hours as illustrated in Fig. 4.22(c) and (d). With increased mission search time of four hours, we observed that myopic search performance started to resemble that of linear search.

4.3.11 Case 11: 15 April, Location 2, Time Late, $\tau = 24$ hrs; Search Time, $T = 1$ to 4 hours

Next, we looked at location 2 where the mean surface current speed affecting the drifter was 60% more than location 1. For $T = 1$ hour, linear search continued to perform better for all ranges of sweep width as shown in Fig. 4.23(a). When T was increased to two hours, the crossover point where linear search started to perform better than myopic search shifted to

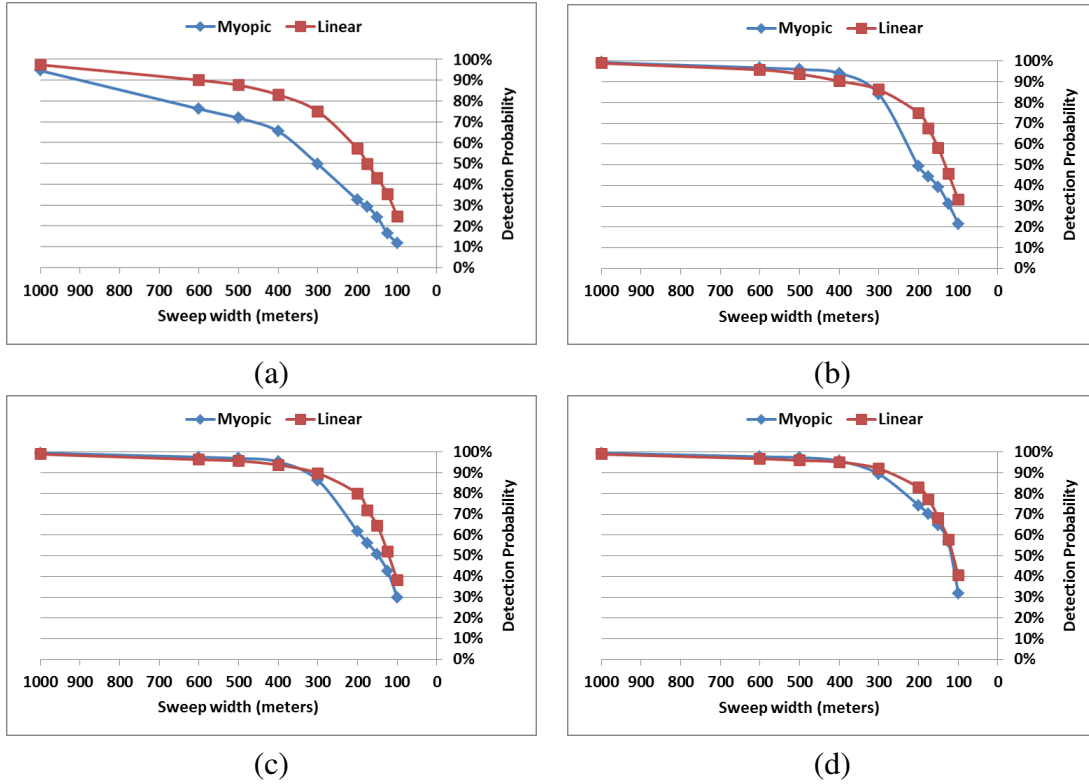


Figure 4.22: Search mission results at location 1 for $\tau = 36$ hours, W ranging from 100 m to 1,000 m, and for varying search time with (a) $T = 1$ hour, (b) $T = 2$ hours, (c) $T = 3$ hours and (d) $T = 4$ hours. Myopic search performed considerably worse than linear search at $T = 1$ hour but started to resemble linear search performance as T was increased to 4 hours

around W of 500 m. As mission duration increased further, the crossover point was shifted down to a W that was between 400 and 300 m as shown in Fig. 4.23(b), (c) and (d). In addition, we observed that when T was increased to three hours, myopic search had about 10% improvement in detection probability at W of 300 m but minimal improvement for W at 200 m and below. On the contrary, the improvement of detection probability for linear search was more gradual and reaching its plateau towards $T = 4$ hours.

4.3.12 Case 12: 15 April, Location 2, Time Late, $\tau = 36$ hrs; Search Time, $T = 1$ to 4 hours

Similar analysis can be seen from Fig. 4.24(a) as we note that myopic search continued to perform much worse than linear search at $T = 1$ hour but quickly regained the search performance when T was increased to two hours. Crossover point was again seen at W between 400 and 300 m as illustrated in Fig. 4.24(b). Another point to note is that the improvement in myopic search for W at 300 m and below was seen to improve, with the highest improvement of about

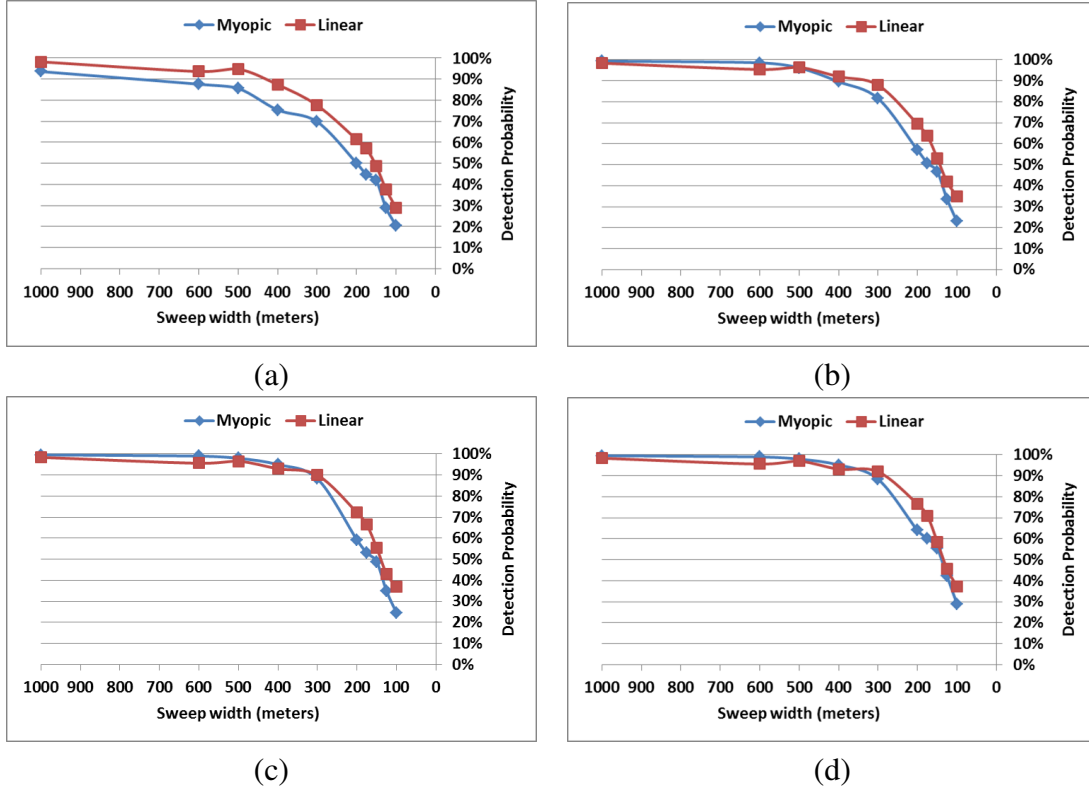


Figure 4.23: Search mission results at location 2 for $\tau = 24$ hours, W ranging from 100 m to 1,000 m, and for varying search time with (a) $T = 1$ hour, (b) $T = 2$ hours, (c) $T = 3$ hours and (d) $T = 4$ hours. Linear search performed better at $T = 2$ hours at W of about 500 m. This crossover point shifted down to a W of between 400 and 300 m as T increased to 3 hours

10% registered for W at 200 m when comparing between Fig. 4.24(b) and (c). As T was further increased to four hours, the improvement of detection probability for W less than or equal to 200 m was marginal, indicating that both linear search and myopic search were starting to reach their respective plateaus in performance.

4.4 Effects of Weibull Probability Distribution Function

Throughout the analysis of both the potential flow model and historical data sets, the noise data generated from the Weibull PDF was fixed at a scale factor $\lambda = 1.0$ and a shape parameter, $\gamma = 1.5$ for each coordinate as described in Section 3.2.3. In addition, the analysis carried out in Sections 4.2 and 4.3 points to a nonlinear relationship between the detection probability and the reduction of sweep width from 300 m down to 100 m. The hypothesis was, therefore, that if the 500 particles are spread farther apart from their mean value (i.e., by increasing the scale factor), there would be a proportionate reduction in detection probability. As such, we generated

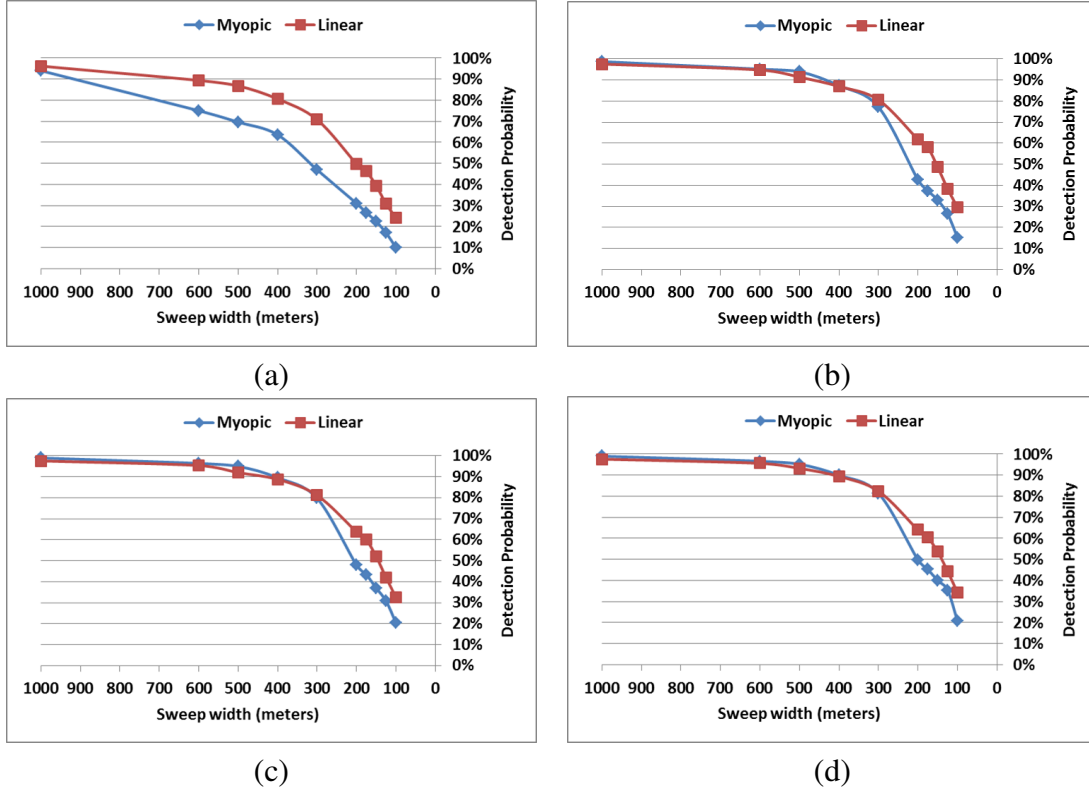


Figure 4.24: Search mission results at location 2 for $\tau = 36$ hours, W ranging from 100 m to 1,000 m, and for varying search time with (a) $T = 1$ hour, (b) $T = 2$ hours, (c) $T = 3$ hours and (d) $T = 4$ hours. Linear search continued to dominate at $T = 1$ hour. Same crossover point was observed at W between 400 and 300 m for T greater than 1 hour

a new set of noise data by increasing the scale factor λ by 10% to 1.1 while keeping the shape parameter, γ , unchanged. Next, we used the new noise data and ran the simulations for the drifter starting at location 1 with a sweep width ranging from 300 m to 100 m and a time late, $\tau = 24$ hours. The results obtained validated the relationship between particle spreading and detection probability. As illustrated in Fig. 4.25, a 10% increase in λ was able to have an effect of reducing the overall detection probability by an average of 22.5% between the two data sets.

Next, we used the “Trendline” function in MS Excel to determine if the plots show a linear or non-linear relationship. For search time T equal to 1 hour (See Fig. 4.26(a)), the detection probability curves for sweep width from 300 m to 100 m pointed to a linear relationship with a high R^2 value of 0.936 for the original myopic data and 0.983 for the myopic data with λ increased to 1.1. Increasing T to two or three hours also indicated a linear relationship between sweep width and detection probability with a high R^2 value of more than 0.92. However, the linearity relationship was not evident when T was increased to 4 hours as shown in Fig. 4.26(b).

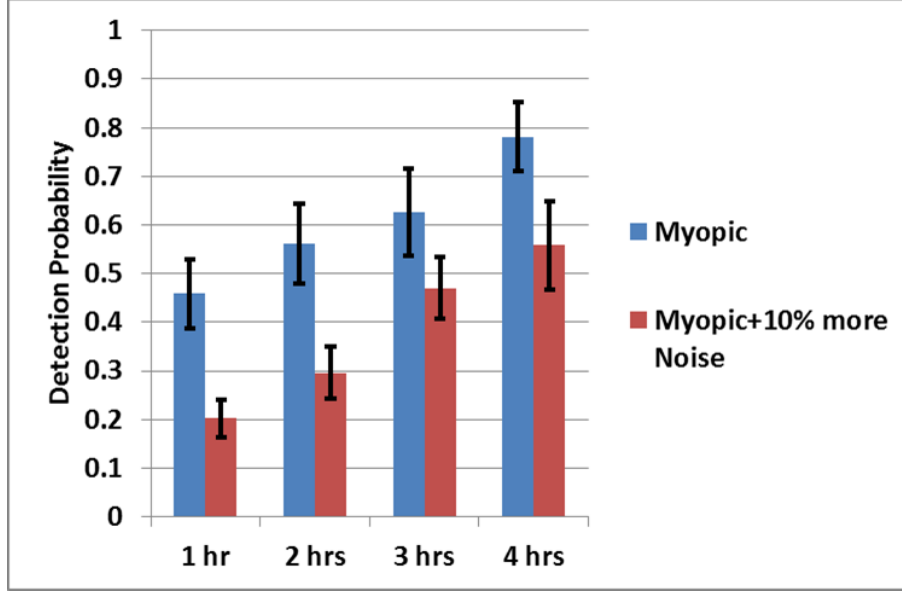


Figure 4.25: Comparison of detection probability between the original myopic data at location 1 with $\tau = 24$ hours and when the scale factor of the Weibull PDF was increased by 10%

A quadratic function was used instead to produce a high R^2 value of 0.9821 for the original myopic data and 0.965 for the myopic data with λ increased to 1.1.

If we refer back to Fig. 4.21(a), we note the nonlinear relationship for $T = 1$ hour started at a sweep width of 400 m instead of 300 m. So, if we had used the results starting from a sweep width of 400 m, we would be able to obtain a quadratic function to explain the nonlinear drop in detection probability. For $T = 4$ hours, using the data set from sweep width of 300 m onwards was sufficient to show the nonlinear drop in detection probability. As such, the nonlinear reduction in detection probability seen at lower sweep widths can be attributed to a confluence of factors used in the simulation, namely, the Weibull PDF parameters, the sensor sweep width as well as the amount of search duration available.

4.5 Effects of High/Low and High/High Wind/Current Events

References are made to the work carried out by Williams in 2007 in analyzing the High/Low Wind/Currents events in the Persian Gulf. For 15 April, it was characterized as a High Wind, Low Current event. In other words, the Northern Persian Gulf region was experiencing low surface currents but relatively strong offshore and alongshore winds on 15 April. This observation was consistent with the mean surface current speed obtained from the SWAFS data set. For a time late, $\tau = 36$ hours, location 1 registered a mean surface current speed of 0.2725

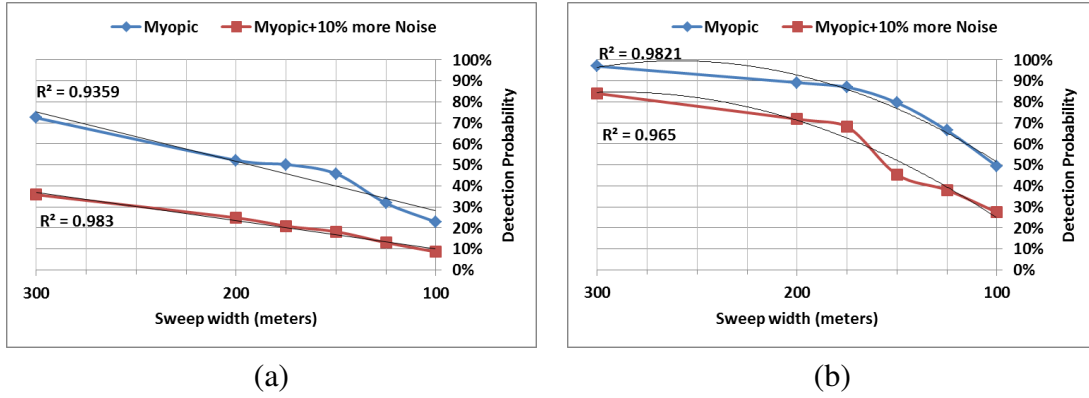


Figure 4.26: Comparison of increasing the scale factor of the Weibull PDF at location 1 by 10% for (a) $T = 1$ hour and (b) $T = 4$ hours. Blue diamonds denote the original myopic search results with $\lambda = 1.0$ while red squares denote the myopic search results with $\lambda = 1.1$

m/s based while location 2 registered a mean surface current speed of 0.4315 m/s. Given that location 2 was relatively nearer to land mass, it was more susceptible to strong offshore winds as compared to location 1. As shown in Subsection 4.3.3 and 4.3.4, the 58% difference in U had minimal impact on search performance when large sensor sweep width were used at the two locations. However, if the sweep width was reduced to 100 m, myopic search suffered an additional 17% drop in search performance due to the increased U . On the other hand, linear search only encountered a 10% drop in search performance.

Similarly, 15 July was characterized as a High Wind and High Current event. The combine effects of high surface currents and high offshore winds created a mean surface current speed at location 2 (See subsection 4.3.7) that was 74% stronger than location 1. We observed the same minimal impact to search performance when the sweep width was large. However, when the sweep width was reduced to 100 m as described in subsection 4.3.8, the difference in search performance between both locations was only a reduction of about 5% in detection probability for both myopic and linear search. Thus, we noted that by using a relatively large sweep width, we were able to nullify the fluctuations in mean surface current speeds. But when the sweep width was reduced to 100 m, the effects of the wind and surface currents were not straight forward. Additional research work (e.g., run simulations for multiple start locations and different time periods) will be required to investigate and understand how the search performance is being affected by the High/Low Wind/Current events and the use of small sensor sweep widths.

Table 4.4: Calculated p -value result for the 10 different sweep widths used in the simulation runs. For each sweep width, there are 32 pairs of mean detection probability comparing between myopic search and linear search. Each mean detection probability result was obtained by performing 500 simulation runs. Blank entries denote p -values of < 0.00001 , denoting statistically statistical difference between myopic and linear search methods.

W (m)	1000	600	500	400	300	200	175	150	125	100
p -value	0.337	0.089	0.071	0.062	0.003	–	–	–	–	–

4.6 Statistical Analysis on Historical Data Set

Similar to Section 4.2, we use the Student’s T-test method to carry out a hypothesis testing on the results obtained from the historical data set. The null hypothesis, H_0 , remains unchanged and is defined as “both myopic search and linear search have the same detection performance.” The alternative hypothesis, denoted as H_1 , is defined as “the detection performance between myopic search and linear search are distinctively different.” For the result to be deemed significant, we chose the α -value to be 0.05 or 5%. The p -value result for all 10 sweep width values are calculated and listed in Table 4.4. We observed that for $W \geq 400$ m, the p -value is greater than α and thus we do not reject the null hypothesis (i.e., there is no evidence to infer that the alternative hypothesis is true). For $W \leq 300$ m, the calculated p -value is very much less than α . Given that the p -value is highly significant, there is overwhelming evidence to infer that the alternative hypothesis is true and we reject the null hypothesis (i.e., the detection performance between myopic search and linear search are likely to be different). The statistical analysis showed that as W gets larger, the search performance between the two strategies will likely yield the same results. This conclusion echoes the analysis carried out in Section 4.2.

The mean detection probabilities for the 320,000 simulation runs performed on the historical data set are presented in Fig. 4.27. The plots reaffirmed the nonlinear decline in detection probability as the sweep width is reduced linearly. The nonlinearity starts at about W of 400 m to 300 m and, as described in Section 4.4, is closely related to a number of contributing factors. For example, if we increase the scale factor used in the Weibull PDF, it increases the spread of the 500 particles from their mean and thus reduces the overall detection probability. Given the same sweep width values and the amount of search time available, the nonlinearity will start at higher sweep width ranges.

Next, we plot out the mean detection probabilities and their corresponding standard error bars as shown in Fig. 4.28. The immediate take away is that linear search has a better mean search

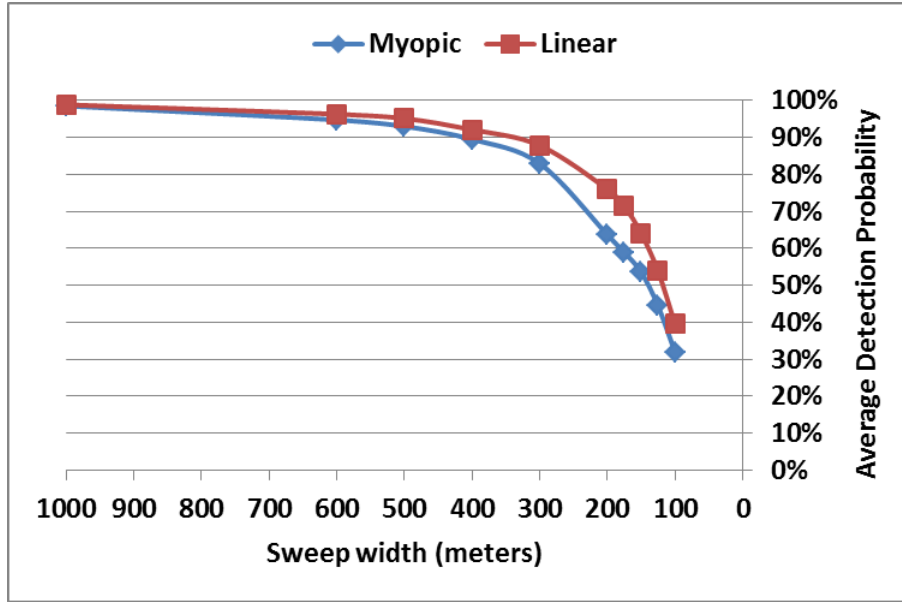


Figure 4.27: Total mean probability of detection between myopic search and linear search. The nonlinearity drop in detection probability for both search strategies was observed to start from a W of about 400 m to 300 m

performance than myopic search for all values of W . For $W \geq 400$ m, there are overlaps between the two standard errors obtained for both linear and myopic search with myopic search registering an average standard error of 1.36% as compared to an average standard error of 0.54% for linear search. For $W \leq 300$ m, there are no overlaps between the two standard errors even when myopic search and linear search registered a higher mean standard error of 3.15% and 1.99%, respectively.

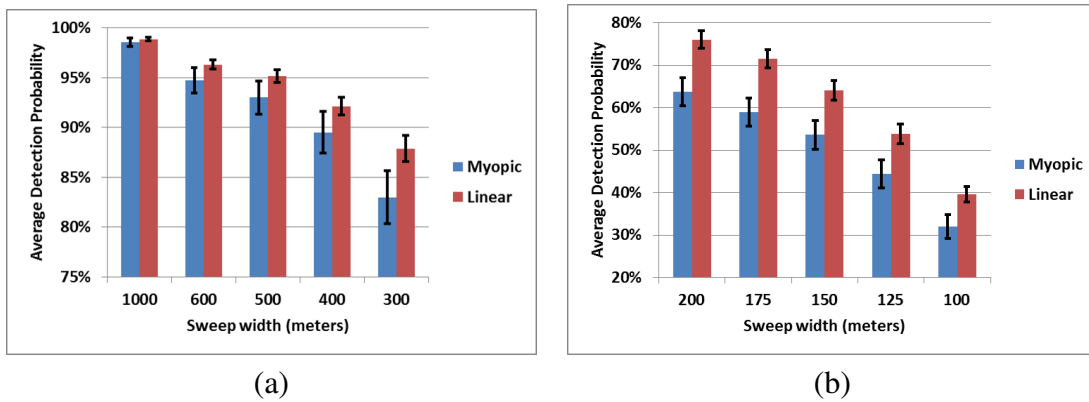


Figure 4.28: Comparison of the total mean probability of detection with error bars for myopic search and linear search. The error bars overlap at $W \geq 400$ m. Even with a higher standard error for $W \leq 300$ m, there are no overlaps between the two search strategies

CHAPTER 5:

Conclusions and Future Work

While today's sea mines are more technologically advanced and stealthy, they are also more costly and require an in-depth knowledge of the various influence parameters and programming to allow them to strike the intended target at the opportune time. However, a rogue nation that has been sanctioned or one with little resources to bear against a superior navy is likely to leverage cheap and low technology contact mines [35] that, when deployed through indiscriminate mine laying, will be able to quickly deter or deny enemy access to its littoral environments.

The mine warfare mission has never been more important, with at least 30 countries having the ability to manufacture naval mines and about 20 of those exporting the mines they produce. All in all, more than 50 nations have attained a certain degree of mining capability and given their flexibility and cost-effectiveness, mines make attractive weapons in asymmetric warfare. The cost of producing and laying a mine is usually anywhere from 0.5% to 10% of the cost it takes to remove it. In addition, it can take up to 200 times as long to clear a minefield as compared to the time it takes to lay it. In summary, countering terrorist mining is very difficult and time consuming. However, combining the right tools (Ocean and Search models) and adding a little bit of innovation to it, a tough problem may be broken down to a much simpler problem that is much easier to solve.

5.1 Simulation Model

The search and localization of a drifting object have significant operational relevance in numerous contexts and the motivation for this topic was derived from a BAA released by ONR in 2011 looking for innovative solutions in the localization and tracking of surface or near-surface drifting mines. Given the prevalence of unmanned systems as well as the advancement of computational resources and analytic methodologies, the stage is set for the development of integrated models incorporating both oceanographic and search-theoretic methods. The presented work shows that a single unmanned system equipped with a capable detector can effectively respond to a time-delayed cue for an object under the influence of ocean surface currents. Monte Carlo simulations were carried out on a simplified ocean current model as well as historic ocean currents data obtained from SWAFS. The stochasticity of real-world ocean environments was addressed by introducing perturbations according to Weibull noises at each time interval, which

resulted in an expanding area enclosing the likely locations of the drifting object. Search of this simulated expanding area was conducted by using either a naïve linear spiral-out search pattern or an optimized myopic allocation of search effort, and the probability of detection as a function of relevant parameters was investigated.

5.2 Findings

Various factors can affect the search outcome, and this study has shown that the speed of the surface current (relative to the search speed) and the sensor sweep width of the searcher have dominant influence on the probability of detection of the object. When the sweep width is large (i.e., greater than or equal to 400m), linear search and myopic search exhibit similar probability distribution curves. As the sweep width is reduced linearly down to 100m, we observed a nonlinear decrease in detection probability, which is attributed to the scale and shape factors used in the Weibull Noise. The use of large sweep width settings has also shown to be able to nullify the drop in detection probability brought on by an increase in surface current speeds. For a 58% to 74% increase in surface current speed, there was minimal change to the detection probability when the sensor sweep width used was large. However, when the sweep width was reduced to 100m, the drop in detection probability can range from 10% to 17% for a 58% increase in surface current speed to as little as 5% for a 74% increase in surface current speed. Further simulation runs will be required to fully map out the relationship between small sweep width and the change in surface current speeds. In essence, the presented work highlights the fact that for most cases, straightforward linear search usually performs better than myopic search in both detection probability and search mission time required to successfully find the drifting object.

5.3 Areas of Future Research

This study has clearly demonstrated the value proposition that ocean models and search-theoretic methods can bring in countering surface or near-surface drifting mine threat. While the naïve linear search performed better than the optimized myopic search effort in this study, there are several other more advanced search algorithms (e.g., multiscale adaptive search [29]) that have been developed for both single and multiple searchers scenario. In addition, both ocean models and search Tactical Decision Aids are usually two separate and distinct models and additional efforts will be required to encapsulate these integrated models into a user interface for decision support software. This thesis focused on two-dimensional flow models to address the surface or near-surface mine threat. Future extensions that examine full three-dimensional flow mod-

els that include a myriad of surface and bottom mines would also enhance the viability of the presented approach.

THIS PAGE INTENTIONALLY LEFT BLANK

REFERENCES

- [1] L. Stone *et al.*, “Search analysis for the underwater wreckage of Air France Flight 447,” in *2011 Int. Conference on Inform. Fusion (FUSION)*, (Chicago), pp. 1–8, 2011.
- [2] IAMSAR, “Int. aeronautical and maritime search and rescue manual,” tech. rep., Int. Maritime Organization and the Int. Civil Aviation Organization, 2009.
- [3] T. R. Bernitt and S. J. Tangredi, “Mine warfare and globalization: Low-Tech warfare in a high-tech world,” *Globalization and Maritime Power*, 2002.
- [4] M. Chambers, “Energy (A Special Report); Just in Case: What happens if Iran blocks the Strait of Hormuz? U.A.E. is weighing some projects to keep the oil flowing,” in *Wall Street J.*, (NY), pp. R.7–R.7, 2007.
- [5] V. Clark, “Sea Power 21: Projecting decisive joint capabilities,” *United States Naval Inst. Proc.*, vol. 128, no. 10, pp. 32–41, 2002.
- [6] K. R. Hibbert, *A need for systems architecture approach for next generation mine warfare capability*. Monterey, CA: M.S. thesis, Naval Postgraduate School, 2006.
- [7] R. H. Dekmejian, “International politics of the Persian Gulf,” *Choice*, vol. 49, no. 6, p. 1145, 2012.
- [8] T. M. Melia, *Damn the torpedoes: A short history of U.S. naval mine countermeasures, 1777-1991*, vol. 4. Washington, D.C.: Dept. of the Navy, Naval Historical Center, 1991.
- [9] M. McCarton, *One hundred years of sweeping: A historical review of the efficacy of organic to the battleforce mine countermeasures*. Arlington, VA: Warfare Systems Directorate, Naval Sea Systems Command, 2000.
- [10] M. Zwolski, “The history of mining,” *Surface Warfare*, vol. 23, no. 3, pp. 20–21, 1998.
- [11] C. Srivastava, “Mine warfare,” *SPs Naval Forces*, vol. 1, p. 198, 2010.
- [12] R. M. Reynolds, “Physical oceanography of the Gulf, Strait of Hormuz, and the Gulf of Oman—Results from the Mt Mitchell expedition,” *Marine Pollution Bulletin*, vol. 27, pp. 35–59, 1993.

- [13] P. G. Thoppil and P. J. Hogan, "A modeling study of circulation and eddies in the Persian Gulf," *J. of Physical Oceanography*, vol. 40, no. 9, pp. 2122–2134, 2010.
- [14] S. M. Abdelrahman and F. Ahmad, "A note on the residual currents in the Arabian Gulf," *Continental Shelf Research*, vol. 15, no. 8, pp. 1015–1022, 1995.
- [15] S. A. R. Sultan and N. M. Elghribi, "Temperature inversion in the Arabian Gulf and the Gulf of Oman," *Continental Shelf Research*, vol. 16, no. 12, pp. 1521–1544, 1996.
- [16] M. H. Azam *et al.*, "3D model application to study residual flow in the Arabian Gulf," *J. of Waterway, Port, Coastal, and Ocean Engineering*, vol. 132, no. 5, pp. 388–400, 2006.
- [17] M. Zhu and B. W. Atkinson, "Observed and modelled climatology of the land-sea breeze circulation over the Persian Gulf," *Int. J. of Climatology*, vol. 24, no. 7, pp. 883–905, 2004.
- [18] C. L. Williams, *Environmental impact on the northern Persian Gulf: A mine drift and chemical spill study centered on Iraq's oil terminals using Navy's ocean-atmospheric physical and chemical models*. Monterey, CA: M.S. thesis, Naval Postgraduate School, 2007.
- [19] F. Yao and W. E. Johns, "A HYCOM modeling study of the Persian Gulf: 1. Model configurations and surface circulation," *J. of Geophysical Research. Oceans*, vol. 115, no. C11, pp. 15323–15333, 2010.
- [20] Y. Alosairi *et al.*, "Mixing and flushing in the Persian Gulf (Arabian Gulf)," *J. of Geophysical Research. Oceans*, vol. 116, no. 3, p. n/a, 2011.
- [21] S. A. Swift and A. S. Bower, "Formation and circulation of dense water in the Persian/Arabian Gulf," *J. of Geophysical Research*, vol. 108, no. C1, pp. 1–4, 2003.
- [22] S. J. Benkoski *et al.*, "A survey of the search theory literature," *Naval Research Logistics*, vol. 38, pp. 469–494, Aug. 1991.
- [23] A. R. Washburn and R. Hohzaki, "The diesel submarine flaming datum problem," *Military Operations Research*, vol. 6, no. 4, pp. 19–30, 2001.
- [24] F. Bourgault *et al.*, "Optimal search for a lost target in a bayesian world," *Field and Service Robotics (STAR Springer Tracts in Advanced Robotics)*, vol. 24, pp. 209–222, 2006.

- [25] T. H. Chung and J. W. Burdick, "Analysis of search decision making using probabilistic search strategies," *IEEE Trans. on Robotics*, vol. 28, no. 1, pp. 132–144, 2012.
- [26] A. R. Washburn, *Search and detection*. Topics in Operations Research Series, INFORMS, 4th ed., 2002.
- [27] L. D. Stone, *Theory of optimal search*. Academic Press, 2nd ed., 1989.
- [28] C. Kim, *The effect of sensor performance on safe minefield transit*. Monterey, CA: M.S. thesis, Naval Postgraduate School, 2002.
- [29] A. Hubenko *et al.*, "Multiscale adaptive search," *IEEE Trans. on Systems, Man and Cybernetics, Part B: Cybernetics*, vol. 41, no. 4, pp. 1076–1087, 2011.
- [30] P. C. Chu *et al.*, "Satellite data assimilation for improvement of naval undersea capability," *Marine Technology Society J.*, vol. 38, no. 1, p. 12, 2004.
- [31] C. Horton *et al.*, "Operational modeling: Semienclosed basin modeling at the Naval Oceanographic Office," *Oceanography*, vol. 5, no. 1, pp. 69–72, 1992.
- [32] R. C. Rhodes *et al.*, "Navy real-time global modeling systems," *Oceanography*, vol. 15, no. 1, pp. 29–43, 2002.
- [33] P. C. Chu, "Statistical characteristics of the global surface current speeds obtained from satellite altimetry and scatterometer data," *IEEE J. of Selected Topics in Applied Earth Observations and Remote Sensing*, vol. 2, no. 1, pp. 27–32, 2009.
- [34] D. C. Montgomery, *Design and analysis of experiments*. John Wiley and Sons Inc, 7th ed., 2009.
- [35] J. A. Boutilier and S. J. Tangredi, "Globalization and maritime power," *Int. J.*, vol. 58, no. 4, pp. 741–743, 2003.

THIS PAGE INTENTIONALLY LEFT BLANK

Initial Distribution List

1. Defense Technical Information Center
Ft. Belvoir, Virginia
2. Dudley Knox Library
Naval Postgraduate School
Monterey, California
3. Marine Corps Representative
Naval Postgraduate School
Monterey, California
4. Directory, Training and Education, MCCDC, Code C46
Quantico, Virginia
5. Marine Corps Tactical System Support Activity (Attn: Operations Officer)
Camp Pendleton, California
6. Professor Jeffrey D. Paduan
Naval Postgraduate School
Monterey, California
7. Professor Peter C. Chu
Naval Postgraduate School
Monterey, California
8. Professor Timothy H. Chung
Naval Postgraduate School
Monterey, California
9. LCDR Meng Wee Joses Yau
Naval Postgraduate School
Monterey, California
10. Mr. Ronald E. Betsch
MIW Program Manager
Naval Oceanographic Office
Stennis Space Center, Mississippi